A response surface methodology approach for the removal of methylene blue dye from wastewater using sustainable and cost-effective adsorbent

Process Safety and Environmental Protection 184 (2024) 129–150

Contents lists available at ScienceDirect

Process Safety and Environmental Protection

journal homepage: www.journals.elsevier.com/process-safety-and-environmental-protection

A response surface methodology approach for the removal of methylene blue dye from wastewater using sustainable and cost-effective adsorbent

Kehinde Shola Obayomi [a,b,*], Sie Yon Lau [a], Michael K. Danquah [c], Jianhua Zhang [b], Tung Chiong [a], Oluwatobi Victoria Obayomi [d], Louise Meunier [e], Mohammad Mahmudur Rahman [f]

[a] Department of Chemical Engineering, Curtin University, CDT 250, 98009 Miri, Sarawak, Malaysia
[b] Institute for Sustainable Industries and Liveable Cities, Victoria University, Werribee, VIC 3030, Australia
[c] Department of Chemical and Biomolecular Engineering, University of Tennessee, Knoxville, TN, 37996, United States
[d] Department of Microbiology, Landmark University, Omu-Aran, Kwara State, Nigeria
[e] Department of Chemical Engineering, Queen's University, Kingston K7L 3N6, Canada
[f] Global Centre for Environmental Remediation (GCER), College of Engineering, Science and Environment, The University of Newcastle, Callaghan, NSW 2308, Australia

ARTICLE INFO

Keywords:
Graphene oxide
Calcium-oxide nanoparticles
Green synthesis
Organic dye
Selective adsorption
Response surface methodology

ABSTRACT

Potable water availability is becoming increasingly challenging due to increasing level of global population and industrial revolution. The disproportionate use of methylene blue (MB), particularly in industrial applications, is a growing concern due to its high resistance to biodegradation and propensity to taint aquatic environments. In this study, we developed novel eco-friendly calcium oxide nanoparticles from eggshells and fishbones (CaONPs-ES and CaONPs-FB) and decorated them on graphene oxide (GO) surfaces. Both nanocomposites (CaONPs-ES@GO and CaONPs-FB@GO) were characterized using state-art-instruments and used for the removal of MB from aqueous solutions. transmission electron. Additionally, the adsorptive performance of CaONPs-ES@GO and CaONPs-FB@GO and their mechanisms of interaction with MB were investigated. BET, SEM/EDX, and XPS results revealed that the CaONPs-ES@GO and CaONPs-FB@GO were predominantly mesoporous, with surface areas of 112 m^2/g and 108 m^2/g, respectively. The temperature-dependent adsorption isotherms and kinetics of CaONPs-ES@GO and CaONPs-FB@GO towards MB were consistent with Redlich-Peterson and pseudo-second-order models, respectively. The Redlich-Peterson model demonstrated an adsorption similarity to the Freundlich model more than the Langmuir model, suggesting the dominance of a heterogeneous multilayer mechanism. The synthesized nanocomposites exhibited high reusability and stability for MB adsorption (>70%) even after 10 successive adsorption-desorption cycles. Thermodynamic evaluations revealed that the adsorption process was spontaneous, endothermic, and physically driven. The nanocomposites exhibited an outstanding selective adsorption behaviour towards MB from the mixture containing MB/RhB and MB/MO with separation efficiency of 99.10% and 77.34% for CaO-ES@GO, and 61.23% and 47.81% for CaO-FB@GO respectively. The particulate interaction mechanisms within the nanocomposites primarily involved π-π interaction, hydrogen bonding, pore-filling, and electrostatic attraction. The cost analysis revealed that the developed nanocomposites are more economical for treating MB in a large-scale application. Based on the statistical analysis using response surface methodology (RSM), the contributing effects of temperature and adsorbent dosage, as well as the single effect of pH, had the most significant impact on MB removal. The nanocomposites demonstrate a promising potential for sustainable MB treatment.

1. Introduction

Freshwater is an essential component of human life. However, these freshwater resources are polluted due to the increasing global population, urbanization, and industrialization, with various types of domestic and industrial effluents (Bhagat et al., 2023). According to the

* Corresponding author at: Department of Chemical Engineering, Curtin University, CDT 250, 98009 Miri, Sarawak, Malaysia; Institute for Sustainable Industries and Liveable Cities, Victoria University, Werribee, VIC 3030, Australia.
E-mail addresses: obayomiks@postgrad.curtin.edu.my, obayomikehindeshola@gmail.com (K.S. Obayomi).

https://doi.org/10.1016/j.psep.2024.01.106
Received 17 November 2023; Received in revised form 9 January 2024; Accepted 31 January 2024
Available online 3 February 2024

AQUASTAT report of the United Nations Educational, Scientific and Cultural Organization (UNESCO), approximately 56% of global freshwater withdrawal is discharged as household, agricultural, and industrial wastewater. Moreover, about 70% of wastewater is discharged into the natural environment without prior treatment (Peramune et al., 2023). In recent years, wastewater contaminated with synthetic dyes has garnered significant attention worldwide due to its persistence, low biodegradability, and potential for environmental and health hazards due to their carcinogenic, mutagenic, and toxic nature (Dahlan et al., 2023). Furthermore, these dyes impede sunlight penetration, negatively impacting photosynthesis and plant growth, increasing chemical and biochemical oxygen demand, and subsequently diminishing the aesthetic quality of water bodies (Obayomi et al., 2023a). Additionally, dyes can exacerbate respiratory issues and cause skin irritation (Dan et al., 2023). Owing to the recalcitrant nature of these dyes in the environment, their removal from water bodies necessitates the development of novel treatment strategies (Ahmadian and Jaymand et al., 2023). Consequently, the urgent demand for innovative, cost-effective, eco-friendly, and sustainable wastewater treatment strategies has become increasingly crucial for ensuring the long-term availability of clean water.

Among the various approaches for dye treatment, adsorption techniques are widely accepted (Liu et al., 2022). Recently, researchers in wastewater remediation have shifted their focus to the use of adsorbent materials based on sustainability, rapid adsorption rate, economic feasibility, and high adsorptive performance (Vo et al., 2022). A limited number of notable materials, such as activated carbon (Vasiraja et al., 2023), metal-organic frameworks (MOFs) (Hu et al., 2023a), metal oxide nanoparticles (Sachin et al., 2023), and carbon nanomaterials (Qasem et al., 2022), have been explored for dye-contaminated water treatment. However, adsorbent-based graphene oxide (GO) nanocomposites have garnered considerable interest due to their impressive adsorptive performance compared to other reported adsorbents.

Over the past few years, the ability of GO to adsorb pollutants from aqueous solutions has been extensively studied, owing to its high surface area and hydrophilicity (Shaheen et al., 2023). GO contains oxygen-containing functional groups, such as carboxylic, hydroxyl, carbonyl, and epoxide groups, which provide reactive sites for modification and facilitate strong interactions, such as electronic attraction, between the adsorption of positively charged cationic dye molecules and the GO surface (Moradi et al., 2022a). However, GO exhibits an edge-to-center distribution of hydrophilic and hydrophobic domains due to the presence of oxidized groups and unoxidized graphitic lattice, respectively (Lotfy et al., 2023). Additionally, GO can agglomerate in water, resulting in a reduction of its surface area and a decrease in its pollutant removal capabilities. GO agglomeration can also hinder rapid mass movement due to the reassembly of graphene nanosheets as a result of strong π–π stacking interactions, making its separation from wastewater after pollutant adsorption difficult and costly (Anuma et al., 2021; Obayomi et al., 2023b). In order overcome these limitations, GO can be chemically modified to enhance its separation capabilities, maintain its adsorption behavior, and reduce van der Waals interactions between GO sheets to increase its surface area by minimizing undesired GO sheet stacking (Januário et al., 2022).

Recently, the use of metal oxide nanoparticles (NPs) as adsorbent materials in wastewater treatment has gained significant attention due to their large surface area and small size (Pai et al., 2023). Factors that make nanoparticles effective adsorbents include enhanced permeability, small size, mechanical properties, and numerous active sites with high surface area. The reactivity of a nanomaterial increases relative to its bulk state as its size decreases. These characteristics facilitate their use in wastewater treatment, resulting in improved water quality, recycling, reuse, and purification (Shahraini et al., 2022). Researchers have reported the utilization of various metal NPs, such as zinc oxide (Asjadi et al., 2022), silver (Princy et al., 2023), and titanium oxide (Rheima et al., 2022), iron oxide (Hammad et al., 2022) for dye treatment. Among other NPs, calcium oxide nanoparticles (CaONPs) have attracted the most attention due to their unique properties and potential applications in diverse industries. Calcium oxide (CaO) is particularly appealing because it is cost-effective, highly basic, non-corrosive, eco--friendly, and easy to handle compared to homogenous base catalysts. Moreover, due to their distinctive qualities and environmentally friendly properties, CaONPs are increasingly favored as a method of choice for environmental applications, especially in wastewater treatment. The green synthesis of CaONPs offers numerous advantages in nanoscience and technology, particularly for wastewater treatment applications. Additionally, waste shells, such as eggshells (ES) and fishbones (FB), are significant sources of CaO, which constitutes 95% of calcium carbonate ($CaCO_3$). Consequently, discarded shells represent a considerable amount of waste (Kumar et al., 2022). The green synthesis of CaO using bio-waste materials is an eco-friendly, cost-effect, sustainable and simple process (Sree et al., 2020). Therefore, decorating the GO surface with CaONPs not only combines the advantages of both materials but also introduces novel features and enhances stability.

The adsorptive performance of GO was enhanced by decorating its surface with CaONPs derived from eggshells and fishbones (CaONPs-ES@GO and CaONPs-FB@GO). The novelty of this work lies in the method design for CaONPs preparation from waste eggshells and fishbones incorporated on the GO surface for methylene blue (MB) dye treatment from an aqueous environment, which, to the best of our knowledge, has not been reported previously. This study focuses on: (1) synthesis of novel and sustainable CaONPs-ES@GO and CaONPs-FB@GO nanocomposites via the green route, and characterization of the nanocomposites using advanced techniques such as thermogravimetric analysis (TGA), X-ray diffraction (XRD), transmission electron microscopy (TEM), Fourier transform infrared spectroscopy (FTIR), X-ray photoelectron spectroscopy (XPS), scanning electron microscopy with energy dispersive spectroscopy (SEM/EDS), Brunauer-Emmett-Teller analysis (BET), and atomic force microscopy (AFM); (2) investigation of the effect of contact time, adsorbent dosage, pH, MB initial concentration, temperature, and ionic strength on the adsorptive performance of the developed nanocomposites toward MB in a batch system; (3) Fitting the adsorption experimental data using various isotherm (Langmuir, Freundlich, Temkin, Dubinin-Radushkevich (D-R), Jovanovic, Harkins-Jura, Halsey, and Redlich-Peterson (R-P)) and kinetic (pseudo-first order, pseudo-second order, Elovich, intraparticle diffusion, and Boyd) models, and evaluating the adsorption thermodynamics; (4) Gaining a better understanding of the mechanisms governing the interaction between MB and the nanocomposites; (5) Studying the recyclability and reusability of the nanocomposites toward MB dye after successive cycles, assessing their performance in real-life samples, and evaluating nanocomposites production cost and large-scale MB treatment efficacy; and (6), employing the central composite design (CCD) as an aspect of response surface methodology (RSM) to optimize variables such as temperature, adsorbent dosage, and pH to maximize the targeted response (MB removal).

2. Materials and method

2.1. Materials

Hydrogen peroxide (H_2O_2, 30%), potassium permanganate ($KMnO_4$), graphite (99%), sodium nitrate ($NaNO_3$), hydrochloric acid (HCl, 37%), methylene blue (MB), sulfuric acid (H_2SO_4, 98%), and sodium hydroxide (NaOH, 98%) and of analytical grade were purchased from Sigma-Aldrich and Merck Chemicals. Malaysia.

2.2. Synthesis of calcium oxide nanoparticles (CaO))

The calcium oxide nanoparticles (CaO) was synthesize using the sol-gel method as described in the previous study of Obayomi et al. (2023c). The eggshells (ES) and fishbones (FB) employed in this study were

obtained from Curtin University, Malaysia Kitchen. In order to eliminate dirt and detach the inner membrane from the shell, ES were washed multiple times with distilled water and then immersed in 1% HCl overnight. Thereafter, the ES were sieved, and washed again using water (distilled), dried in an oven for 2 h at 108 °C, crushed to powder, and stored finally in an airtight plastic bag. In order to get rid of undesirable materials, for 30 min, the washed FB were left to boil and thoroughly washed using distilled water, it was then dried in an oven for 12 h at 80 °C, crushed to powder, and placed in a plastic bag for storage. Thereafter, ES and FB powder (20 g each) was dissolved separately in 500 mL beakers that contains 37% of 1 M HCl (400 mL). The solutions were allowed until effervescence stopped (about 6 h), demonstrating the establishment of calcium chloride ($CaCl_2$). Then, 1 M of 98% NaOH (300 mL) was added in a dropwise manner via a burette, which led to the formation of precipitate of calcium hydroxide ($Ca(OH)_2$). It was then centrifuged for 20 min at 3000 rpm. The resulting $Ca(OH)_2$-ES and $Ca(OH)_2$-FB were washed with water (distilled), and dried for 3 h at 80 °C. Finally, $Ca(OH)_2$-ES and $Ca(OH)_2$-FB were subjected to calcination for 1 h at 900 °C, and 1000 °C to develop white calcium oxide nanoparticles (CaONPs-ES, and CaO-FB). The as-synthesized materials were kept in a plastic bag.

2.3. Synthesis of graphene oxide (GO)

The hummer's method reported by obayomi et al. (2023c) in previous study was also followed without modification to develop GO. Here, 90 mL sulfuric acid, 2.5 g sodium nitrate, and 2.5 g graphite powder were taken in a 250 mL beaker and constantly stirred in an ice bath at 10 °C for 2 h to obtain a homogeneous mixture. In order to keep the temperature e of the reaction below 10 °C, potassium permanganate (30 g) was gradually introduced to the mixture in the ice bath at specific time intervals. The mixture was stirred continuously in an ice bath for 2 h. Then, water (150 mL) was gradually added to the brown paste, causing an exothermic reaction to occur that generated heat and brought the temperature of the reaction mixture to approximately 98 °C. Then, mixture was left at room temperature to cool, and afterwards 50 mL hydrogen peroxide was added to it in drops till a golden yellow coloration was observed. Thereafter, mixture underwent centrifugation and washed severally times with distilled water and 5% HCl solutions. Following a wash, it was then filtered, dried overnight in an oven at 60 °C, and as-prepared GO was stored in an airtight container for later usage.

2.4. Synthesis of GO incorporated-CaO

Briefly, CaO-ES (4 g) was measured and added into 100 mL distilled water placed in a 250 mL beaker and was stirred constantly using a magnetic stirrer at room temperature. Thereafter, GO (2 g) was weighed and transferred to the mixture under constant stirring, and the resulting mixture was vigorously stirred for a 3 h period and then placed in an ultrasonicator for 2 h. Following the ultrasonication process, stirring of the mixture continued for additional 2 h to guarantee a homogeneous mixture. Subsequently, the mixture was treated hydrothermally by transferring it to a 100 mL autoclave (Teflon-lined autoclave) for 18 h at 120 °C. Following the procedure, the mixture was kept cooling properly at room temperature before washing numerous times with water (ultrapure) and transferred for drying in an oven for 24 h at 70 °C. Finally, organic materials and impurities were eliminated from the dried sample by calcining it in a muffle furnace for 2 h at 550 °C. The same procedure was repeated for the prepared CaO-FB. The GO incorporating CaO-ES (CaO-ES@GO) and CaO-FB (CaO-FB@GO) nanocomposites were stored in a sealed plastic bag. Moreover, the schematic diagram showing the summary of the preparation is as presented in Fig. 1. The characterization of the developed nanocomposites using state of art techniques to examine their physiochemical properties have been discussed in the supplementary section.

2.5. Batch adsorption studies

Batch adsorption system was carried out at varying temperatures ranging from 298, 308, and 318 K via numerous 250 mL Erlenmeyer flasks containing various MB concentrations (10–50 mg/L). 50 mg of

Fig. 1. Pictorial diagram showing the synthesis of CaO-ES@GO and CaO-FB@GO nanocomposites.

CaO-ES@GO and CaO-FB@GO was introduced into each of the flasks while maintaining the MB dye solutions initial pH value. In order facilitate the adsorption process between adsorbents and MB molecules, the mixture was placed on a shaker (isothermal) at 160 rpm shaker speed for 180 min at constant temperature. The MB samples were analysed at various time intervals before equilibrium was attained using a UV–VIS spectrophotometer (Shimadzu UV-1601 spectrophotometer, Japan) set at 664 nm. Eqs. 1–3 were used to calculate the amount of adsorbed adsorbate at time (t) and at equilibrium, as well as the MB percentage removed at various intervals of time.

$$\%MB \quad removal = \left(\frac{C_o - C_f}{C_o}\right) \times 100 \tag{1}$$

$$q_e = \frac{(C_0 - C_e) \quad V}{W} \tag{2}$$

$$q_t = \frac{(C_0 - C_t) \quad V}{W} \tag{3}$$

Where C_f represents the final MB dye concentration while C_o stands for the initial MB dye concentration in mg/g; W denotes the adsorbents weight (g), V indicates the volume of the dye solution (L), C_t stands for the equilibrium concentration at time, t (mg/g) while C_e stands for the equilibrium concentration.

2.6. Selective adsorptive experiment

The selective sequestration performance of CaO-FB@GO and CaO-ES@GO composites towards cationic and anionic dye was explored. The selective adsorption experiment was conducted using binary mixture of MB/Rhodamine B(RhB) and MB/Methylene orange (MO) at equilibrium conditions. A mixture of RhB and MO (50 mg/L, 50 mL each), was prepared and mixed with 50 mL MB solution in several beakers (250 mL) to form a bi-component dye mixture. Thereafter, 0.04 g/L of the nanocomposites were gradually introduced to the mixture. The mixtures were then positioned and shaken in an isothermal shaker at 160 rpm and 318 K for 60 min. Finally, the absorbance of the binary mixture after and before adsorption were measured using the UV–vis spectrometer at different wavelength (300–800 nm). Furthermore, the separation efficiency (α) of MB in the binary dye mixtures was calculated using Eq. 4:

$$\alpha \quad (\%) = \frac{C_A}{C_A + C_B} \times 100 \tag{4}$$

where $C_A and C_B$ are the remaining dye concentrations in the solution after adsorption.

2.7. Optimization of MB removal

In this research, a subdivision of the response surface methodology (RSM), specifically the central composite design (CCD), amongst others, was employed to investigate the interactions between contributing variables on MB adsorption and to optimize the adsorptive performance of CaO-ES@GO and CaO-FB@GO nanocomposites. The three factors characterizing the CCD are: six centre runs (6 points), two factorial runs (8 points), and two axial runs (6 points), all together leading to 20 experimental runs. The quadratic equation model (optimal predictor), as suggested by the design given in Eq. 5, was employed to correlate the variables and the responses (MB removal).

$$y = \beta_o + \sum_{i=1}^{k} \beta_i X_i + \sum_{i=1}^{k} \beta_{ii} X_i^2 + \sum_{i<j} \beta_{ij} X_i X_j \tag{5}$$

where y stand for the response, β_o stands for the coefficient constant, β_i, β_{ii}, β_{ij}, denote linear, quadratic, and interactive coefficients. The using Design Expert statistical software was employed to carry out the regression analysis in order to measure the statistical significance of the equations obtained from the experimental data. The response variability was estimated using probability value (P-value, with a confidence level of 95%), Fisher's value (F-value), and the correlation coefficient (R^2). Table S1 presents the values of the independent variable range and their coded levels.

3. Results and discussion

3.1. Characterization

3.1.1. TGA/DTG analysis

The weight losses of 4.4% (25–470 °C) and 4.08% (25–452 °C) for CaO-ES@GO and CaO-FB@GO from derivative thermogravimetric (DTG) analyses and thermogravimetric (TGA) are displayed in Fig. 2(a-b), possibly brought on by the breakdown of volatile organic matter and desorption of adsorbed water molecules on the surfaces of CaO-ES@GO and CaO-FB@GO (Liu et al., 2008; Sangon et al., 2021). A temperature rises to 712 and 752 °C resulted in weight losses of approximately 10.5%, and 18.9% respectively for CaO-ES@GO and CaO-FB@GO. These findings may potentially underscore the thermal decomposition of numerous oxygen-containing groups (Zaki et al., 2022). In addition, the CaO-ES@GO and CaO-FB@GO nanocomposites exhibited weight losses of 16.1% and 13.3% between 712–920 °C, and 752–943 °C respectively, due to $CaCO_3$ decomposition (Saleh and Taufik, 2019). The DTG curve of CaO-FB@GO demonstrated the highest decomposition temperature at 712 °C and a series of smaller peaks at 452 and 920 °C, while the maximum decomposition peak temperature of CaO-ES@GO was at 692 °C, with smaller peaks at 445 and 950 °C. The peaks correspond to the decomposition of organic and volatile matters present on the surfaces of CaO and GO (Hussain et al., 2022). The overall loss in weight of CaO-ES@GO and CaO-FB@GO nanocomposites was 30.7% and 36.6% respectively. Collectively, the data suggest that CaO incorporation might have greatly enhanced the thermal stability of CaO-ES@GO and CaO-FB@GO nanocomposites (Maruthupandy et al., 2020).

3.1.2. XRD analysis

The XRD pattern for CaO-ES@GO demonstrates the formation of additional peaks at 25.5°, 27.7°, 38.6°, and 50.8° upon the fusion of CaO-ES onto the surface of GO. Additionally, the result shows that the GO phase peak (100) has slightly shifted from 42.8° to 43.2°, indicating that CaO-ES was deposited satisfactorily on the GO surface (Obayomi et al., 2023). Furthermore, the disappearance of the GO major phase (001) from the XRD pattern of CaO-ES@GO may be accredited to the small quantity of GO introduced into the mixture or due to the presence of interfacial interactions and favourable spread of GO nanoparticles within the matrix (Sajjad et al., 2022). The XRD pattern for CaO-ES@GO demonstrates the presence of peaks at 25.5°, 27.7°, 38.6°, and 50.8° after the deposition of CaO-ES onto the GO surface. It was also noted that the GO phase peak slightly shifted from 42.8° to 43.2°, indicating that CaO-ES had been successfully deposited on the GO surface (Zheng et al., 2023). Furthermore, comparing the XRD patterns of CaO-FB and GO with CaO-FB@GO, a significant change in some peaks was observed, resulting in new peaks formation. The formation of new diffraction peaks at 36.0°, 47.1°, 48.4°, 57.5°, 60.8°, 62.6°, and 64.2° may be due to the hydrothermal synthesis of CaO-FB@GO (Kasirajan et al., 2022). Additionally, the GO sharp peak at 11.58° (002) shifted to 14.7°, while the peak at 42.8° remained unchanged, suggesting the effective loading of CaO-FB in the GO matrix (Singh et al., 2022). The XRD pattern of FB, ES, GO, CaO-ES and CaO-FB have been discussed extensively in the supplementary section (SI).

3.1.3. FTIR analysis

The FTIR spectra of ES, CaO-ES, GO and CaO-ES@GO nanocomposite is shown in Fig. 2(e). The observed FTIR spectra of CaO-ES@GO, in

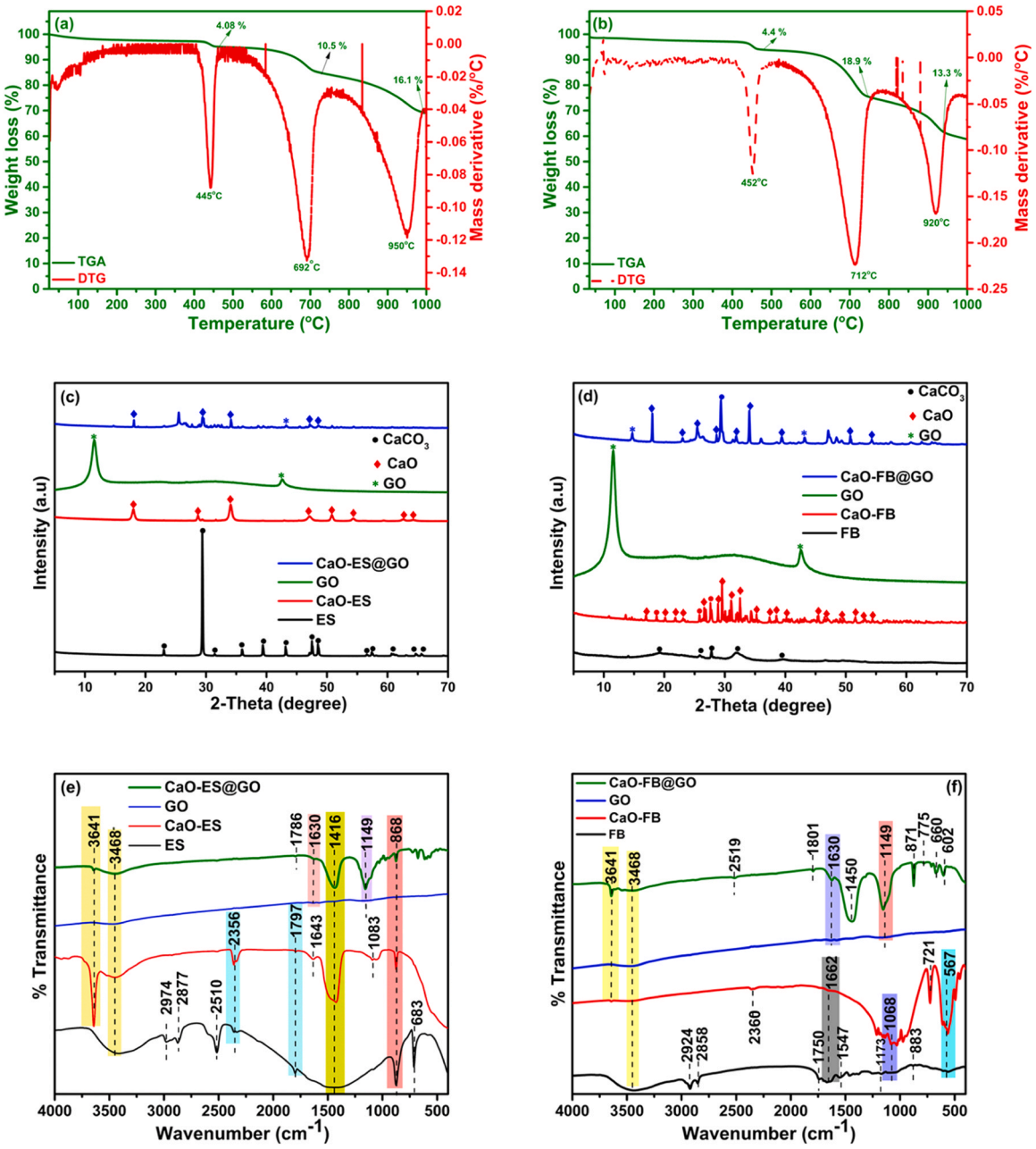

Fig. 2. (a-b) TGA/DTG, (c-d) XRD, and (e-f) FTIR analysis of CaO-ES@GO and CaO-FB@GO nanocomposites.

comparison with GO and CaONPs, confirm the successful deposition of CaO-ES on the GO surface. After deposition, the peaks at 868 cm^{-1}, 3468 cm^{-1}, 3641 cm^{-1} and 1797 cm^{-1} corresponding to Ca-O stretching, C═C, O-H groups in the CaO were detected after the synthesis of CaO-ES@GO nanocomposite (Obayomi et al., 2023c). The absorption bands at 1630, 1416, and 1149 cm^{-1} allotted to C═O, C═C, C-OH, and C-O on the GO were also confirmed to be present in the nanocomposite spectra, corroborating a successful CaO-ES deposition on the surface of GO (Rasheed et al., 2023). The FTIR spectra of FB, CaO-FB, GO, and CaO-FB nanocomposite is represented in Fig. 2(f). The peak located at 1662 cm^{-1} is linked with the C-H bending vibration. The band sited at 1068 cm^{-1} could be allotted to C-N stretching, validating non-degenerate symmetric stretching of the phosphate groups and the existence of amine groups (Obayomi et al., 2023b). The absorption band at 567 cm^{-1} confirms the P-O degenerate bending mode while the peak positioned at 721 cm^{-1} could be ascribed to Ca-O stretching, ratifying the existence of CaO. Comparing the IR spectra before and after the thermal decoration of the GO surface with CaO-FB (CaO-FB@GO), slight modifications in the material functional groups were observed, with some peaks retained, shifted, or disappeared (Zhu et al., 2023). The peaks at 3468 and 3641 cm^{-1} assigned to the functional group O-H on GO and CaO-FB spectra, were retained in the CaO-FB@GO spectrum. The GO spectrum peaks situated at 1630 and 1149 cm^{-1}, corresponding to the stretching vibrations due to C═C bonds of the unoxidized carbon skeleton and the C-O epoxide group, remained after the synthesis of CaO-FB@GO, confirming the presence of GO on the surface of the nanocomposite (Singh et al., 2022). Furthermore, peaks related to CaO-FB were retained, while others shifted. The peaks at 2519 (shifted), 1662, and 1081 cm^{-1} (shifted), corresponding to the carbon dioxide group, C-H bending, and amine groups, were detected on the surface of the nanocomposite (Sharma et al., 2022). The new peak at 1450 cm^{-1}, which formed as a result of the decoration of CaO-FB on GO, could be credited to the C═C bond. The presence of CaO on the CaO-FB@GO surface was confirmed from the peaks located at approximately 871,

775, 660, and 602 cm^{-1} (Rasheed et al., 2023). The discussion on FTIR spectra of FB, ES, GO, CaO-ES, and CaO-FB have also been discussed in the supplementary section.

3.1.4. SEM/EDX analysis

The SEM image of ES, depicted in Fig. 3(a), clearly reveals an irregular, rough, large crystal-like structure with numerous micropores on the surface. The FB exhibits a rough and coarse surface (Fig. 3(b)). The micrograph of CaO-ES in Fig. 3(c) displays an irregular, rough, and flower-like structure with mild agglomeration, while CaO-FB in Fig. 3(d) presents a composition of particles with various spherical masses, aggregated, and porous. The agglomeration of particles can be credited to the calcination of $Ca(OH)_2$ during the preparation step. The GO micrograph, as shown in Fig. 3(e), exhibits a rough, flaky structure and wrinkled surfaces. The wrinkling on the GO surface could be as a result of the interaction between hydrophobic regions within the sheet (Yang et al., 2022). The SEM images of CaO-ES@GO and CaO-FB@GO obtainable in Fig. 3(e-f), demonstrate that the nanocomposites possess a flake-like structure with CaO homogeneously distributed over the surface of GO. The elemental composition of the composites, as depicted in Fig. 3(h-i), shows the presence of C, Ca and O, signifying the successful fusion of CaONPs onto the surface of GO.

3.1.5. TEM/AFM analysis

The TEM images of synthesized CaO-ES, CaO-ES@GO, CaO-FB, CaO-FB@GO, are shown in Fig. 4. The SEM micrographs of CaO-ES, and CaO-FB displayed in Fig. 4(a-b), demonstrate that the particles are made up of weak agglomeration and spherical shape which could results from particle-particle interaction. As revealed in Fig. 4(c-d), the agglomerated surfaces of CaO-ES and CaO-FB diminished after impregnation with GO, while the presence of spherical CaO that was uniformly dispersed on the surface suggests that CaO-ES@GO and CaO-FB@GO were successfully synthesized. The average particle size of CaO-ES@GO and CaO-FB@GO, were calculated to be 38.1 nm and 30.6 nm, respectively. The CaO-ES@GO and CaO-FB@GO nanocomposites surface roughness is presented in Fig. 2(e-f). The AFM images revealed that the CaO-ES@GO (Fig. 2e) surface was smoother than CaO-FB@GO (Fig. 2 f). The surface roughness of CaO-FB@GO may be attributed to the diameter of the pores and surface porosity, owing to CaO distribution on the GO surface (Khalili et al., 2022). The average roughness of CaO-ES@GO and CaO-FB@GO are 110.7 and 224.4, respectively.

3.1.6. BET analysis

The N_2 adsorption-desorption isotherm measurement of CaO-ES, CaO-FB, CaO-ES@GO, and CaO-FB@GO are, presented in Fig. 5. The BET surface area of CaO-ES, CaONPs-FB, CaO-ES@GO and CaO-FB@GO were 61.88, 47.43, 121.14, and 108.23 m^2/g; pore volume of 0.00311, 0.00551, 0.0901, and 0.0411 cm^3/g; and pore diameter of 4.90, 4.55, 3.21, and 3.72 nm, respectively. The improved pore volume and surface area of CaO-ES@GO and CaO-FB@GO could be ascribed to the loading of CaO-ES and CaO-FB onto the surface of GO. The pore diameter values indicate that the materials are predominantly mesoporous (2–50 nm), based on pore classifications. Furthermore, the isotherm curve displayed in Fig. 5 reveals that the nanomaterials exhibit a type IV isotherm curve

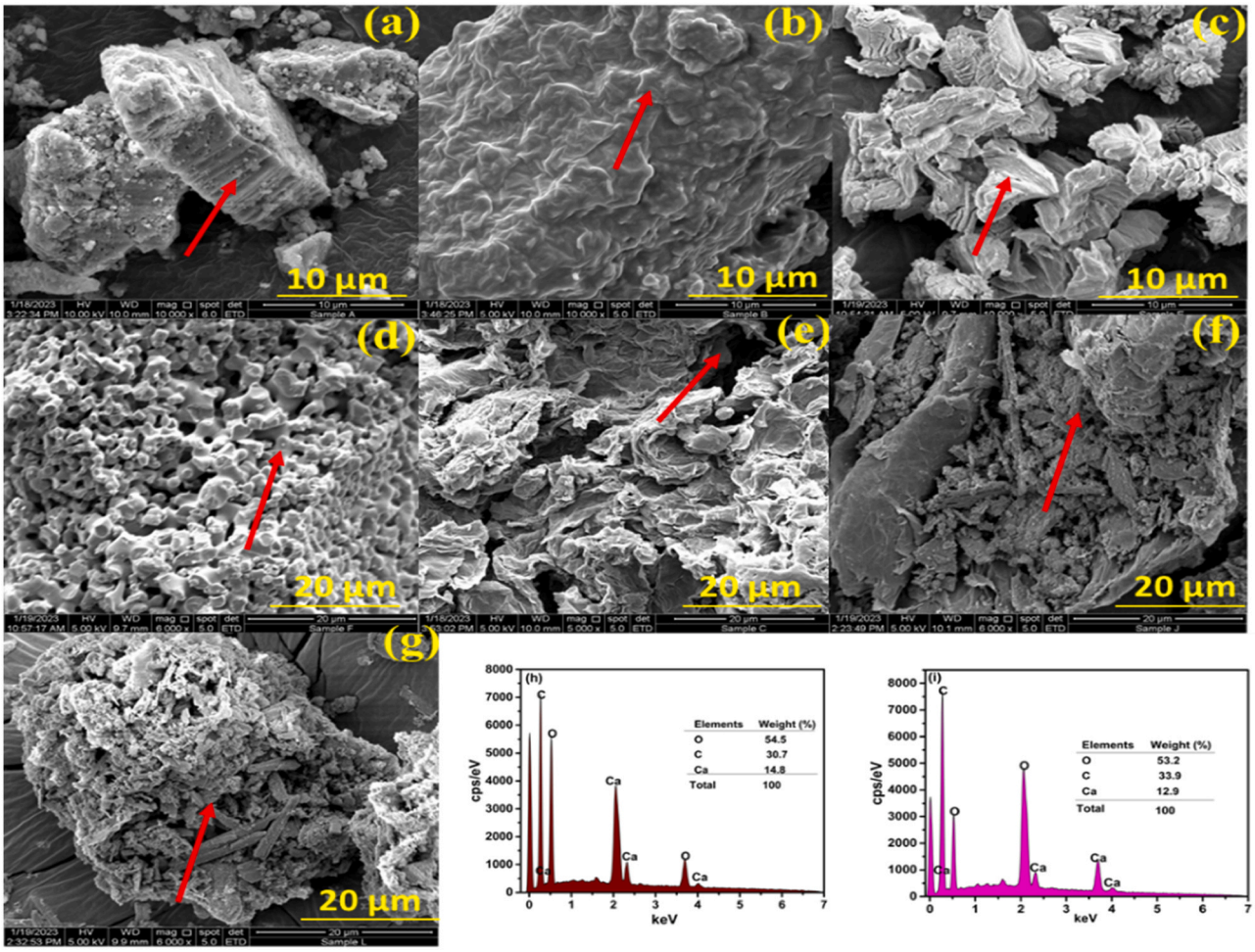

Fig. 3. SEM micrographs of (a) ES, (b) FB, (c) CaO-ES, (d) CaO-FB, (e) GO, (f) CaO-ES@GO, (g) CaO-FB@GO and the elemental composition of (h) CaO-ES@GO, and (i) CaO-FB@GO.

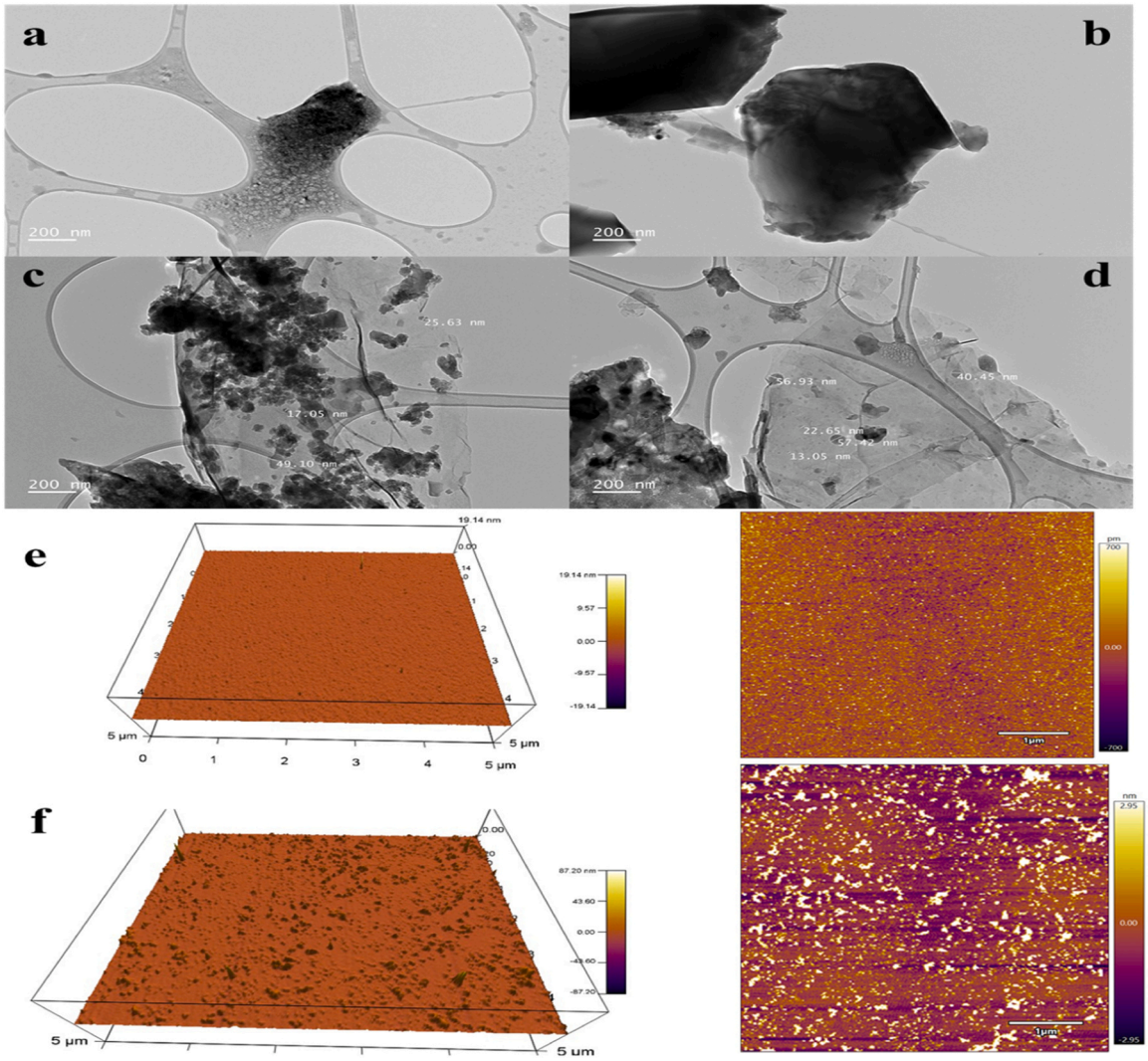

Fig. 4. TEM analysis of (a) CaO-ES, (b) CaO-FB, (c) CaO-ES@GO, and (d) CaO-FB@GO, and AFM analysis of (e) CaO-ES@GO, and (f) CaO-FB@GO nanocomposites.

and H3 hysteresis, based on the IUPAC classification, suggesting that the composite materials are non-porous and rich in mesopores, which are distributed between cracks and corners (Yadav et al., 2022; Mechnou et al., 2023).

3.1.7. XPS analysis

The XPS spectra of CaO-ES@GO and CaO-FB@GO are shown in Fig. 6 (a-b) reveal the presence of calcium, carbon, and oxygen elements, suggesting a successful distribution of CaO-ES and CaO-ES on the GO surface. The deconvolution of the C 1 s peaks for CaO-ES@GO (Fig. 5d) and CaO-FB@GO (Fig. 6c) shows three subpeaks at 284.8, 288.8 and 286.4 eV, corresponding to C–C, C═O and C–O bonds, respectively (García-Soriano et al., 2022). The peak at 284.4 eV reveals the presence of graphene nanosheets in the synthesized composites (CaO-ES@GO and CaO-FB@GO) with the presence of hybridized sp^2 C atom (Chandraraj and Xavier et al., 2023). The O 1 s deconvoluted peaks at 535.7 and 539.4 eV for CaO-ES@GO, (Fig. 5e), correspond to the COO- (formed by oxidation of limited-oxygen) and C═O bonds. The CaO-FB@GO deconvoluted peaks at 533.2 and 531.6 eV (Fig. 5f), could be assigned to C-OH and O-C═O, respectively (Vinayagam et al., 2023). The occurrence of Ca-OH, Ca-O-C, C═O, and COO- bonds in the O 1 s spectra of CaO-ES@GO and CaO-FB@GO may be ascribed to the existence of lattice oxygen atoms, adsorbed surface water, and enhanced structural stability of the fabricated materials (Ibrahim et al., 2023a). The O-species presence in the developed nanocomposites (CaO-ES@GO and CaO-FB@GO) can be attributed to the thermal treatment (Garcia et al., 2022). The Ca 2p for CaO-ES@GO reveals two peaks at 347.8 and 349.5 eV (Fig. 5g), while CaO-FB@GO shows peaks at 347.4 and 351.0 eV (Fig. 5h), which are attributable to a strong double spin-orbit Ca 2p3/2 and Ca 2p1/2. The existence of Ca 2p3/2 and Ca 2p1/2 in CaO-ES@GO and CaO-FB@GO suggests the presence of Ca-OH and Ca-O (Kumar et al., 2022).

3.2. Adsorptive performance

Various adsorption parameters, such as pH, contact time, adsorbent dosage, MB initial concentration, and temperature, influenced the uptake ability of CaO-ES@GO and CaO-FB@GO nanocomposites towards MB removal. The findings are illustrated in Fig. 7(a–b). A rapid increase was observed in the percentage removal values and sorption capacities of nanocomposites towards MB within the first 25 min. These values could be attributed to the presence of more sites for adsorption on the CaO-ES@GO and CaO-FB@GO surfaces that might become saturated as time progressed (Yadav et al., 2023). As time progressed beyond this point, the adsorbents had insufficient active sites to adsorb MB molecules, leading to a slow reduction in the adsorption capacity and percentage removal until equilibrium was attained at 60 min, suggesting that the adsorbents' active sites were saturated (Jawad et al., 2023). The MB removal of 79.8% and 77.2% and sorption capacities of 409.3 mg/g and 395.9 mg/g and 409 mg/g onto CaO-FB@GO and CaO-ES@GO

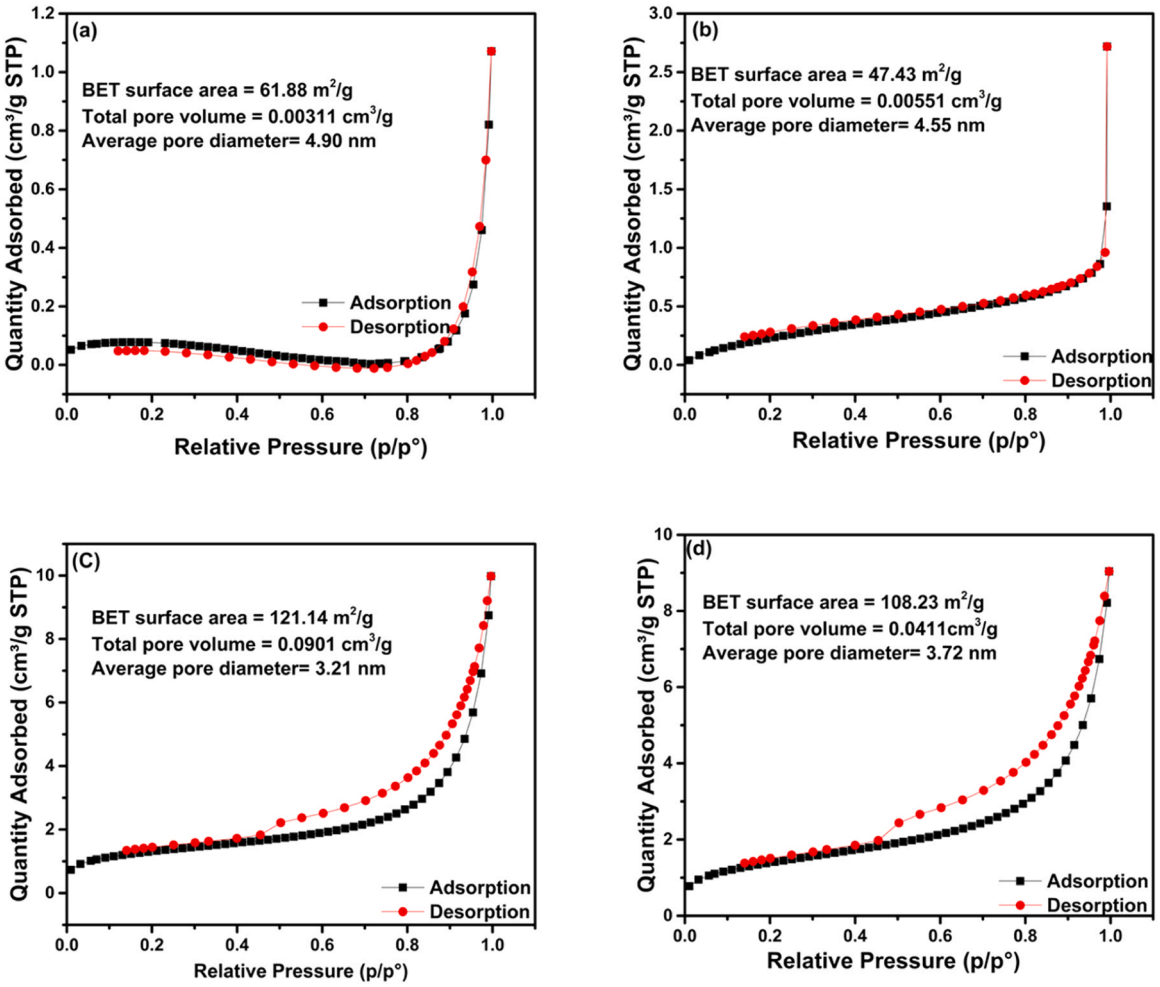

Fig. 5. N_2 adsorption-desorption isotherm of (a) CaO-ES, (b) CaO-FB, (c) CaO-ES@GO, and (d) CaO-FB@GO.

were recorded after the equilibrium position was achieved.

The impact of initial MB concentration on MB removal and adsorption capacity onto CaO-ES@GO and CaO-FB@GO nanocomposites at varied concentrations (10–50 mg/L), 60 min contact time, constant pH 8, and temperature 318 K was examined and shown in Fig. 7(c–d). It is evident from the plots that increasing the MB initial concentrations resulted in a rise in the adsorption capacities and a reduction in the percentage removal of methylene blue onto CaO-ES@GO and CaO-FB@GO nanocomposites. The plots show that MB removal of 98.6% and 95.3% and adsorption capacities of 112.6 mg/g and 101.6 mg/g were observed atCo = 10 mg/L. However, a decrease in percentage removal (79.8% and 77.2%) and significant adsorption capacities (409 mg/g and 395.9 mg/g) were observed atCo = 50 mg/L. The high MB uptake at lower concentrations can be attributed to more active sites on the adsorbent surface ready to adsorb MB dye molecules, while at high concentrations, the active sites are rapidly saturated with a limited number of adsorption sites, leading to their inability to adsorb the MB molecules (Ma et al., 2023; Zhao et al., 2023). Furthermore, the adsorption capacity increase with initial MB increase can be elucidated on the basis that at higher concentrations, driving forces are built up to overcome mass transfer resistance between MB molecules and the CaO-ES@GO and CaO-FB@GO (Jia et al., 2023).

The zeta potential was measured to determine the charges on the nanocomposite surfaces before and after MB adsorption, as shown in Fig. 7(e–f). The values for the pH point of zero charge (PZC) obtained for CaO-ES@GO and CaO-FB@GO were 5.67 and 5.10, respectively. Moreover, the adsorbent surface becomes positively charged when the pH<PZC and negatively charged when the pH>PZC (Alizadeh and Salimi, 2023). At pH < 5.67 and 5.10, the surfaces of the adsorbents experienced the distribution of positive charges due to the protonation of hydrogen ions and the existence of functional groups such as carbonyl. However, at pH > 5.67 and 5.10, the CaO-ES@GO and CaO-FB@GO surfaces became charged negatively as a function of the deprotonation of functional groups, including carboxyl and hydroxyl (Rostamian et al., 2022). Furthermore, after MB adsorption, the PZC values increased to 7.39 and 6.82 for CaO-ES@GO and CaO-FB@GO, respectively. The increase could be attributed to strong electrostatic interactions between the adsorbents and the MB molecules, which support the findings that the sorption performance of CaO-ES@GO and CaO-FB@GO towards MB molecules is greatly influenced by pH (Obayomi et al., 2023d).

The effect of pH on the MB sorption capacity and percentage removal on CaO-ES@GO and CaO-FB@GO were examined, and the plots are shown in Fig. 7(g–h). The pH was varied from 2–11 under optimum conditions (adsorbent dosage = 0.4 g/L, temperature = 318 K, constant time = 60 min, and initial MB concentration = 50 mg/g). The results exhibited an increase in MB adsorption capacity and percentage removal as the pH increased. The MB adsorption capacity and percentage removal on CaO-ES@GO improved steadily from 62.5% and 320.4 mg/g at pH 2 to 98.3% and 503.8 mg/g at pH 8, respectively. The sorption capacity and percentage removal of MB onto CaO-FB@GO increased steadily from 60.2% and 308.4 mg/g at pH 2 to 97.0% and 497.0 mg/g at pH 8, respectively. This is because at lower pH (pH<PZC), the adsorbent's surfaces are protonated due to the hydrogen ions and carbonyl

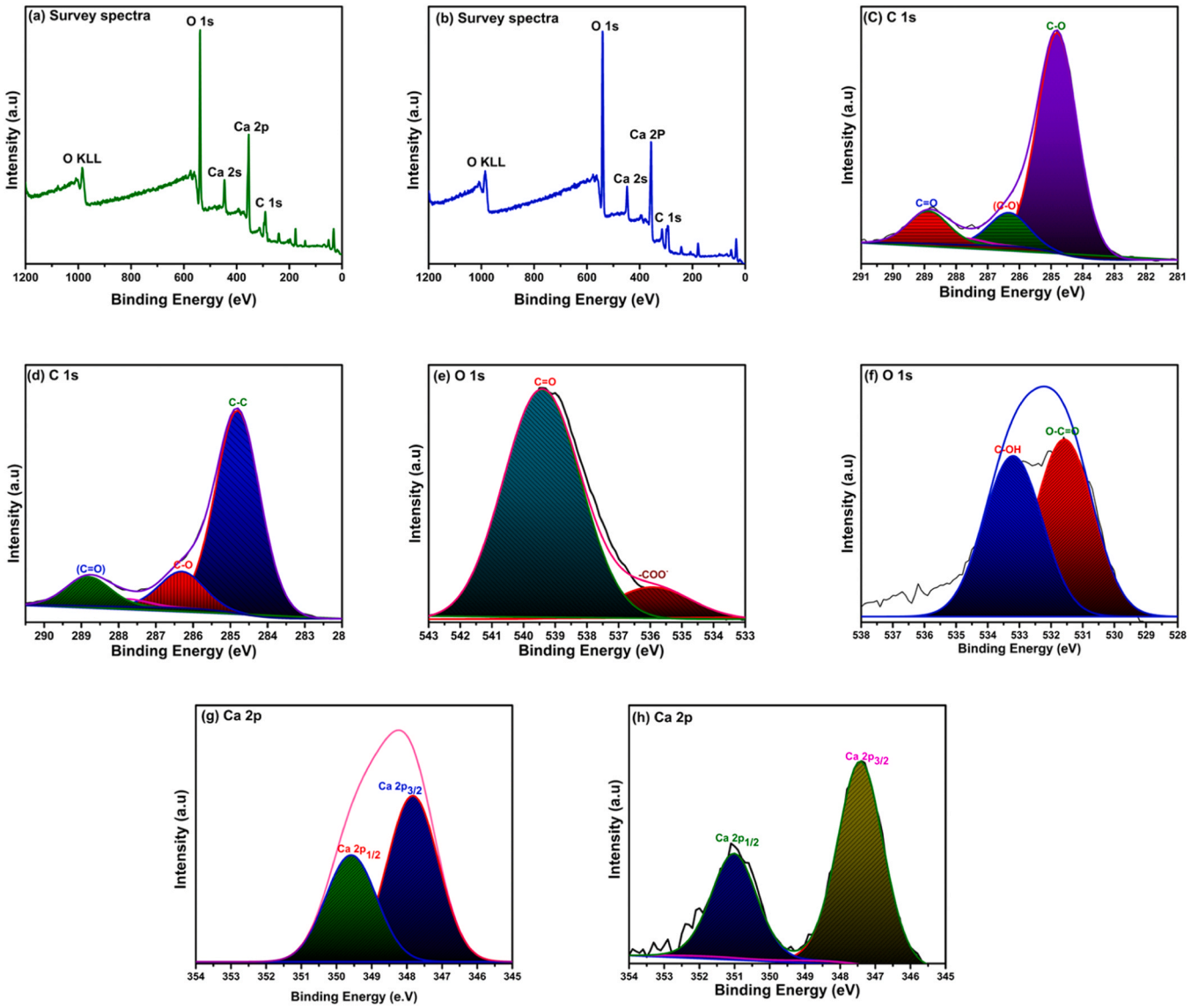

Fig. 6. (a-b) XPS spectra, (c-d) C 1 s, (e-f) O 1 s, and (g-h) Ca 2p of CaO-ES@GO and CaO-FB@GO nanocomposites.

groups, resulting in more competition amongst the positively charged adsorbent surface and positively charged cationic MB for adsorption site interaction, thereby encouraging electrostatic repulsion forces between the MB molecules and nanocomposites, resulting in a significant reduction in MB adsorption capacity and percentage removal (Ullah et al., 2022; Hu et al., 2023b). However, deprotonation of the adsorbent's surfaces was observed at higher pH (pH>PZC) as a result of the existence of oxygen-containing functional groups such as hydroxyl and carbonyl groups, thereby making the adsorbent's surfaces more negatively charged and promoting electrostatic attraction between the positively charged MB molecules and negatively charged adsorbents, thus resulting in a significant increase in MB adsorption capacity and percentage removal (Ndagijimana et al., 2022). In addition, the MB adsorption capacities and percentage removal decreased at low pH due to π-π stacking between the MB aromatic rings and GO as well as hydrogen bond formation between the hydrogen atoms of epoxy, hydroxyl, and carboxyl groups of CaO-ES@GO and CaO-FB@GO and the N atom of MB molecules (Rostamian et al., 2023; Li et al., 2023a). The findings imply that the electrostatic interaction is not the sole mechanism responsible for the adsorption process of MB onto CaO-FB@GO and CaO-ES@GO nanocomposites.

The impact of CaO-FB@GO and CaO-ES@GO dosage on MB removal and sorption capacity was examined by fluctuating the adsorbent dosage from 0.1–0.6 g/L under optimal conditions (constant time = 60 min, pH = 8, initial MB concentration = 50 mg/g, and temperature = 318 K), and the findings are depicted in Fig. 7(i–j). The results revealed that with increasing CaO-ES@GO and CaO-FB@GO and dosage from 0.1–0.4 g/L, the MB percentage removal experienced a significant increase (98.02% and 97.4%), with the optimal dosage being 0.4 g/L. This observation could be due to the gradual increase on the adsorbent's surfaces, which gradually increased as the adsorbent dosage was gradually elevated (Demirezen et al., 2023). However, as the adsorbent dosage gradually increased beyond 0.4 g/L, there was no significant rise in the percentage removal of MB, which might be due to active site saturation or less utilization of the active sites at the specified MB concentration (Wu et al., 2023). Furthermore, increasing the CaO-ES@GO and CaO-FB@GO dosages resulted in a decrease in MB adsorption capacity. This could be attributed to the following reasons; Firstly, the increased sites for adsorption enhanced sorption competition throughout the process of adsorption, and secondly, the stacking effect caused by numerous CaO particles led to some of the adsorption sites on CaO-FB@GO and CaO-ES@GO not being fully contacted by the MB molecules (Liu et al., 2023a).

The influence of adsorption temperature was studied at varied

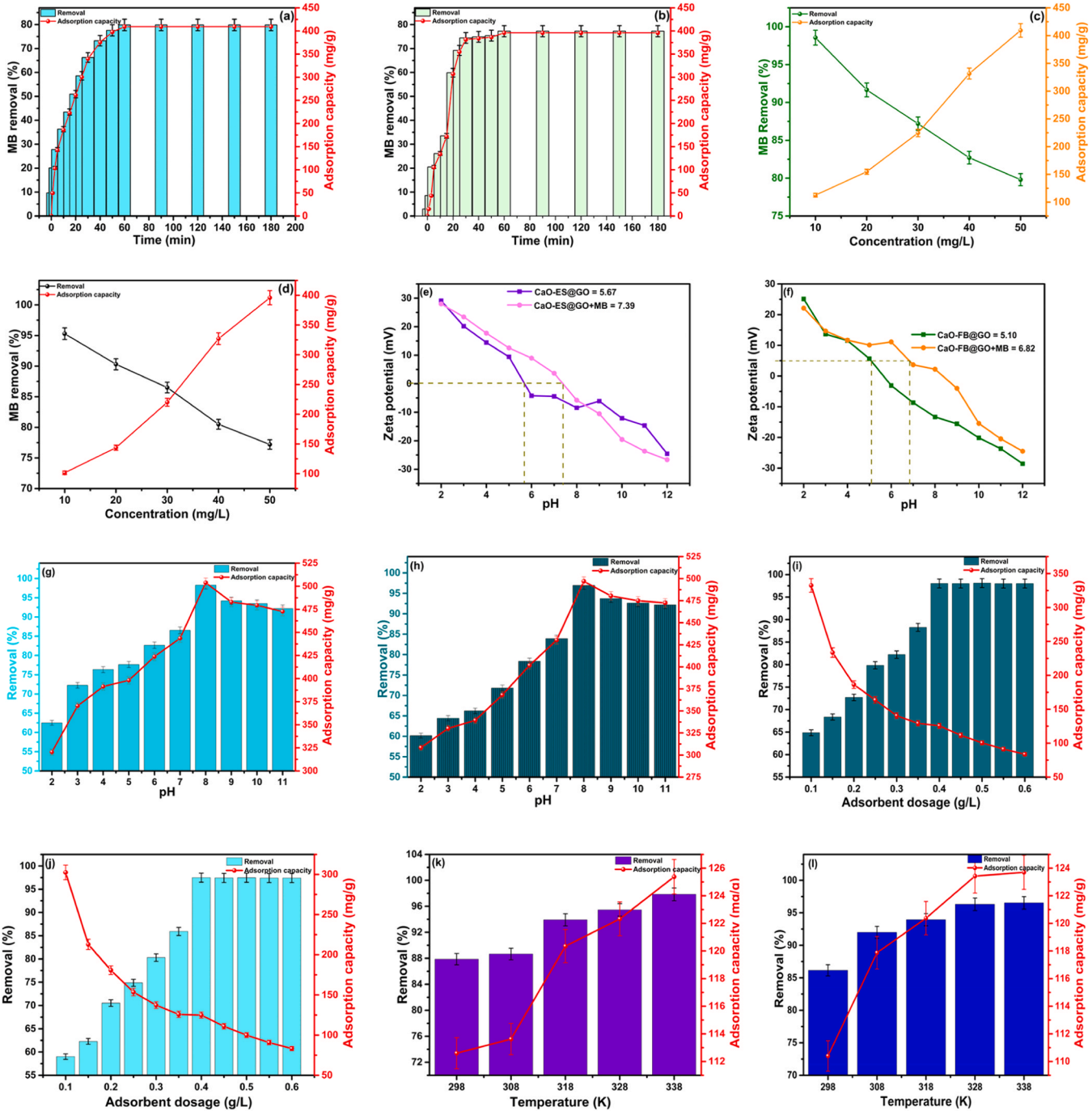

Fig. 7. Adsorptive effect of (a-b) contact time, (c-d) initial MB concentration, (e-f) zeta potential, (g-h) pH, (i-j), adsorbent dosage, and (k-l) temperature on MB adsorption on CaO-ES@GO and CaO-FB@GO nanocomposites.

temperatures from 298–338 K on MB removal efficiency and capacity under optimal conditions (initial MB concentration = 50 mg/g, constant time = 60 min, pH = 8, and adsorbent dosage = 0.4 g/L), as depicted in Fig. 6(k–l). The values obtained revealed that increasing the adsorption temperature resulted in a rise in the removal and sorption capacities of MB onto CaO-ES@GO and CaO-FB@GO, thereby signifying the endothermic nature of the sorption process. The increase in MB adsorption capacity and removal as the temperature is increased may be attributed to the increase in kinetic energy, decreasing the solution viscosity, and promoting the mobility of the molecules of methylene blue on the surfaces of the adsorbent (Pandey et al., 2022).

3.3. Adsorption kinetics

In this study, the adsorption kinetics of MB sorption onto CaO-FB@GO and CaO-ES@GO were examined to identify the mechanism of adsorption and the rate-limiting steps by applying several models, including pseudo-second order, intraparticle-diffusion pseudo-first order, and Elovich and Boyd with their various equations presented in Table S2. The results presented in Table 1 and Fig. S1(a–e) revealed that the adsorption behaviors of CaO-ES@GO and CaO-FB@GO towards cationic MB are more consistent with the pseudo-second-order kinetics than with other models based on higher R^2 and smaller standard error (SE) values. In addition, the experimentally measured adsorption

Table 1
Kinetics model parameters for CaO-ES@GO and CaO-FB@GO nanocomposites.

Models	Parameters	CaO-ES@GO					CaO-FB@GO				
		10 mg/L	20 mg/L	30 mg/L	40 mg/L	50 mg/L	10 mg/L	20 mg/L	30 mg/L	40 mg/L	50 mg/L
Pseudo-first order	$q_{e\ exp}$	12.320	18.490	27.340	40.610	51.260	12.320	18.490	27.340	40.610	51.260
	$q_{e\ cal}$	8.831	14.558	22.405	32.624	46.654	7.500	11.552	19.403	29.613	32.248
	k_1 (min^{-1})	0.121	0.0804	0.139	0.0847	0.0826	0.241	0.0949	0.0838	0.0456	0.0476
	R^2	0.968	0.965	0.929	0.980	0.930	0.943	0.982	0.976	0.982	0.975
	SE	0.121	0.132	0.386	0.140	0.262	0.255	0.0967	0.101	0.0743	0.0868
Pseudo-second order	$q_{e\ exp}$	12.320	18.490	27.340	40.610	51.260	12.320	18.490	27.340	40.610	51.260
	$q_{e\ cal}$	10.686	19.199	30.526	38.226	50.858	11.613	16.000	21.780	35.610	43.900
	k_2 (g mg min^{-1})	0.00454	0.000838	0.00134	0.000516	0.000220	0.0161	0.00250	0.00105	0.000288	0.000302
	R^2	0.999	0.997	1.000	0.999	0.998	1.000	1.000	0.999	0.999	0.998
	SE	0.00803	0.0105	0.00295	0.00251	0.00356	0.00142	0.00295	0.00395	0.00393	0.00301
Elovich	α (mg $g^{-1}min^{-1}$)	117.721	45.926	306.409	182.647	92.723	574.995	422.294	169.859	119.305	341.136
	β (g/mg)	0.0721	0.0366	0.0327	0.0179	0.0129	0.115	0.0466	0.0281	0.0164	0.0159
	R^2	0.888	0.938	0.938	0.957	0.964	0.841	0.939	0.940	0.970	0.962
	SE	7.0767	9.931	11.0882	16.666	21.00924	5.523	7.748	12.670	15.102	17.566
Intraparticle-diffusion	k_{ip} (mg g^{-1} $min^{-0.5}$)	4.237	9.402	10.129	19.0786	27.390	2.511	6.888	11.801	22.0627	23.203
	C	47.927	43.441	105.636	127.0273	91.876	88.929	90.0304	96.549	99.961	164.626
	R^2	0.698	0.831	0.801	0.841	0.879	0.623	0.776	0.803	0.902	0.911
	SE	8.804	12.716	15.326	24.805	30.0387	6.383	11.325	17.727	21.418	21.236
Boyd	B	0.117	0.0816	0.141	0.0849	0.0848	0.200	0.0887	0.0887	0.0497	0.0481
	D_i (10^{-11} m^2/s)	5.879	4.777	5.231	3.657	3.331	5.212	5.101	4.444	5.643	4.987
	R^2	0.959	0.960	0.921	0.977	0.927	0.949	0.988	0.988	0.984	0.980
	SE	0.169	0.164	0.469	0.167	0.307	0.274	0.0864	0.0864	0.0848	0.0924

capacity (qe, exp) is closer to the acquired theoretical adsorption capacity (qe, cal) towards the pseudo-second order. The Elovich equation offered a further visualization of the variance in adsorption energies among adsorptive sites, which directly relates to their heterogeneous character. The decrease in the adsorption (α) and desorption (β) rates with increasing MB initial concentrations, as shown in Table 1, suggests the feasibility of the uptake of MB by CaO-ES@GO and CaO-FB@GO. Moreover, the higher values of α establish that the rate of adsorption is higher than the rate of desorption during the process of adsorption (Alotaibi et al., 2023). The intraparticle-diffusion plots (qt vs. t0.5) at different concentrations presented in Fig. S1(d) demonstrate three stages. In the first stage, which is on the steep sides of the plots, the adsorption pattern suggests that most of the molecules of MB were adsorbed rapidly on the outer surfaces of CaO-ES@GO and CaO-FB@GO, which was attributed to the fast mass transfer rate in the diffusion boundary layer (Shimizu et al., 2023). However, after the attainment of equilibrium position, the poor intra-particle diffusion rate of MB molecules by CaO-ES@GO and CaO-FB@GO delayed the adsorption process during the second stage (Du et al., 2023). Finally, the adsorption behavior of CaO-ES@GO and CaO-@GO towards MB occurs on the active sites of the outer and inner surfaces, resulting in a final equilibrium stage. This equilibrium stage was attained when the intraparticle diffusion process takes longer due to extremely low residual adsorbate and a concurrent decrease in adsorption sites. This led to the conclusion that intraparticle diffusion and surface adsorption might happen simultaneously in MB adsorption (Debnath et al., 2023). As observed from the plots (Fig. S1(d)), the intraparticle-diffusion plots for MB adsorption on CaO-ES@GO and CaO-FB@GO does not cut through the origin, indicating that external mass transfer may be involved and that the intraparticle is not the primary mechanism involved in the adsorption process. The Boyd plots depicted in Fig. S1(e) show that the MB adsorption linear plots also did not cut through the origin, suggesting that both the external mass transfer and intraparticle diffusion govern the sorption rate-limiting steps (Akdemir et al., 2022).

3.4. Adsorption isotherm

The adsorption isotherm was employed in this study to examine the adsorption molecules distribution between the adsorbate and adsorbent under equilibrium adsorption conditions and understand the mechanism underlying the sorption process. The adsorption equilibrium data were modelled by eight isotherms, namely Freundlich, Redlich-Peterson (R-P), Dubinin-Radushkevich (D-R), Langmuir, Halsey, Temkin, Jovanovic, and Harkins-Jura models, and their linear equations are presented in Table S1. The isotherm plots are shown in Fig. S2, and the suitable model to the adsorption process was chosen based on the high correlation coefficient value (R^2), smaller sum of square errors (SSE), and smaller values for the hybrid fractional error function (HYBRID). The results presented in Table 2 revealed that the sorption process of MB onto CaO-ES@GO and CaO-FB@GO could be best explained using the R-P model based on their R^2 (closer to unity) and smaller SSE and HYBRID values in comparison to other studied models. The Redlich-Peterson model incorporates aspects of the Freundlich and Langmuir models, leading to a hybrid model that may be employed in both homogeneous and heterogeneous systems, displaying significant adaptability. However, based on the (<1) values, the MB uptake onto CaO-ES@GO and CaO-FB@GO was majorly dominated by multilayer adsorption mechanisms, and this was characterized by the adsorption behavior of the Freundlich model. The multilayer adsorption behavior assumes that the number of MB molecules adsorbed is not limited by surface area, but molecule stacking may also occur. The multilayer adsorption mechanism based on the R-P model was further supported by the Harkins-Jura and Halsey models. Furthermore, the MB adsorption capacity calculated based on the Langmuir model at varying temperatures (298, 308, and 318 K) for CaO-ES@GO (500.0, 532.9, and 621.02 mg/g) surpassed that of CaO-FB@GO (454.6, 510.2, and 570.8 mg/g). The high sorption capacity of CaO-

Table 2
Adsorption isotherm parameters for MB adsorption on CaO-ES@GO and CaO-FB@GO.

Isotherms	Parameters	CaO-ES@GO			CaO-FB@GO		
		Temperature (K)			Temperature (K)		
		298	308	318	298	308	318
Langmuir	Q_m (mg/g)	500.000	532.91	621.026	454.55	510.20	570.83
	K_L (L/mg)	0.148	0.182	0.581	0.319	0.809	2.497
	R^2	0.947	0.975	0.955	0.968	0.977	0.986
	SSE	0.0798	0.0533	0.0467	8.242	5.699	2.988
	HYBDRID	11.233	10.678	8.766	11.662	10.783	8.456
Freundlich	K_F (mg/g) (L/mg)$^{1/n}$	98.331	110.986	192.983	141.429	180.418	276.503
	1/n	0.589	0.593	0.365	0.444	0.423	0.259
	R^2	0.990	0.998	0.968	0.984	0.993	0.997
	SSE	0.00431	0.000995	0.00132	0.00458	0.00274	0.00118
	HYBDRID	1.412	1.898	1.991	0.0891	0.0561	0.0234
Temkin	K_T (L/mg)	1.724	1.973	2.718	4.326	7.514	12.114
	b_T (J/mol)	18.956	19.298	30.967	24.788	25.701	41.420
	R^2	0.965	0.978	0.926	0.957	0.966	0.976
	SSE	0.269	0.207	0.383	48.515	43.468	36.448
	HYBDRID	12.441	15.676	10.789	13.331	12.677	12.213
D-R	q_s (mg/g)	312.283	333.323	318.120	307.988	338.841	360.146
	K_{ad} (mol^2/J^2) 10^{-7}	4.391	3.684	0.473	1.560	0.878	0.158
	E (kJ/mol)	1.0670	1.165	3.250	1.790	2.387	5.623
	R^2	0.873	0.909	0.818	0.841	0.889	0.916
	SSE	3838.297	2767.461	9973.750	49.322	44.231	39.195
	HYBDRID	20.0211	18.678	14.440	25.678	22.812	19.768
Jovanovich	$q_{m,\ Jv}$ (mg/g)	105.0840	111.193	128.779	123.657	137.674	155.156
	K_{Jv} (L/g)	-0.143	-0.159	-0.190	-0.136	-0.173	-0.224
	R^2	0.978	0.973	0.983	0.984	0.993	0.997
	SSE	0.0490	0.0637	0.0393	0.0752	0.0561	0.0142
	HYBDRID	5.616	5.221	2.898	2.671	1.701	1.691
Harkins-Jura	A_{HJ} (g^2/L)	12671.637	13486.0675	23386.999	18071.386	20228.501	36356.894
	B_{HJ} (mg^2/L)	1.00499	0.944	0.905	1.00592	0.859	0.781
	R^2	0.986	0.971	0.997	0.991	0.980	0.972
	SSE	0.00507	0.00209	0.00144	5.830	1.147	1.479
	HYBDRID	3.556	3.455	3.111	6.701	6.432	6.110
Halsey	K_H (mg/L)	2428.904	2818.415	182562.886	6907.265	22279.159	26935.347
	n_H	1.699	1.687	2.743	2.250	2.370	3.862
	R^2	0.990	0.998	0.969	0.984	0.993	0.997
	SSE	0.000229	0.000128	0.000108	0.00663	0.00413	0.00324
	HYBDRID	0.981	0.771	0.645	1.0451	0.964	0.7896
R-P	β_{RP}	0.411	0.407	0.635	0.556	0.578	0.741
	A (L/g)	98.330	110.986	192.983	141.431	180.419	276.503
	R^2	0.980	0.995	0.990	0.990	0.997	1.00
	SSE	0.0000153	0.00000575	0.0000120	0.000349	0.000145	0.0000624
	HYBDRID	0.212	0.511	0.641	0.0454	0.0233	0.0221

ES@GO could be attributed to the presence of more negatively charged carboxyl and hydroxyl groups, which are responsible for the adsorption of more cationic MB molecules via strong electrostatic attractions. In addition, CaO-ES@GO had a larger pore volume than CaO-FB@GO, which promoted more MB molecules adsorption to diffuse and have access to more of the pores of CaO-ES@GO, thereby promoting higher adsorption capacity towards the cationic MB molecules (Li et al., 2023b). Further, the MB adsorption energies (E) values were 1.067, 1.165, and 3.250 kJ mol-1 for CaO-ES@GO and 1.790, 2.387, and 5.623 kJ/mol for CaO-FB@GO, respectively. This demonstrates that the sorption behavior of MB was ruled majorly by physical adsorption (E < 8 kJ/mol) through a weak van der Waals force between the adsorbate and adsorbent (Kim et al., 2023).

3.5. Thermodynamics evaluation

The adsorptive performance of CaO-ES@GO and CaO-FB@GO towards MB were evaluated at various temperatures (298–318 K) to determine the adsorption character. The thermodynamic parameters such as standard Gibbs free-energy change (DG°), enthalpy change (DH°), and entropy change (DS°) were evaluated from the temperature-dependent plots presented in Fig. 8(a-b). The DG° is equation given as;

$$\Delta G = \Delta G^o + RT\ln K^o_{Equilibrium} \quad (6)$$

Since, the free energy change (ΔG) becomes insignificant as the adsorption process reaches equilibrium, Equ. 6 therefore becomes;

$$-\Delta G^o = RT\ln K^o_{Equilibrium} \quad (7)$$

The connection between ΔG°, ΔS° and ΔH° can be defined as:
ΔG° = ΔH° -TΔS° (8)

$$\ln K^o_{Equilibrium} = -\frac{\Delta H^o}{RT} + \frac{\Delta S^o}{R} \quad (9)$$

$$K^o_{Equilibrium} = \frac{(K_L \times M_w \times 1000) \times [C^o]}{\gamma} \quad (10)$$

where $K^o_{Equilibrium}$ stands for the dimensionless thermodynamic equilibrium constant, K_L stands for the Langmuir constant, K_L (L/mg), M_w stands for the MB molecular weight (319.85 g/mol), [C]° represents the standard concentration of the MB (1 mol/L) and γ is the coefficient activity of MB in solution (dimensionless). Since the MB dye solution was much diluted, the activity of coefficient (γ) is considered unitary. The values of the thermodynamic parameters summarized in Table 3, showed that the adsorption behaviour of CaO-ES@GO and CaO-FB@GO towards MB was feasible and spontaneous judging from the negative ΔG° values obtained at various temperatures (Chen et al., 2020; Lv et al., 2022). The positive values of ΔH° demonstrate the endothermic character of the sorption process. However, ΔH° values < 40 kJ/mol suggest physical adsorption but ΔH° values > 40 kJ/mol predicts chemical adsorption. The ΔH° values of MB adsorption on CaO-ES@GO and

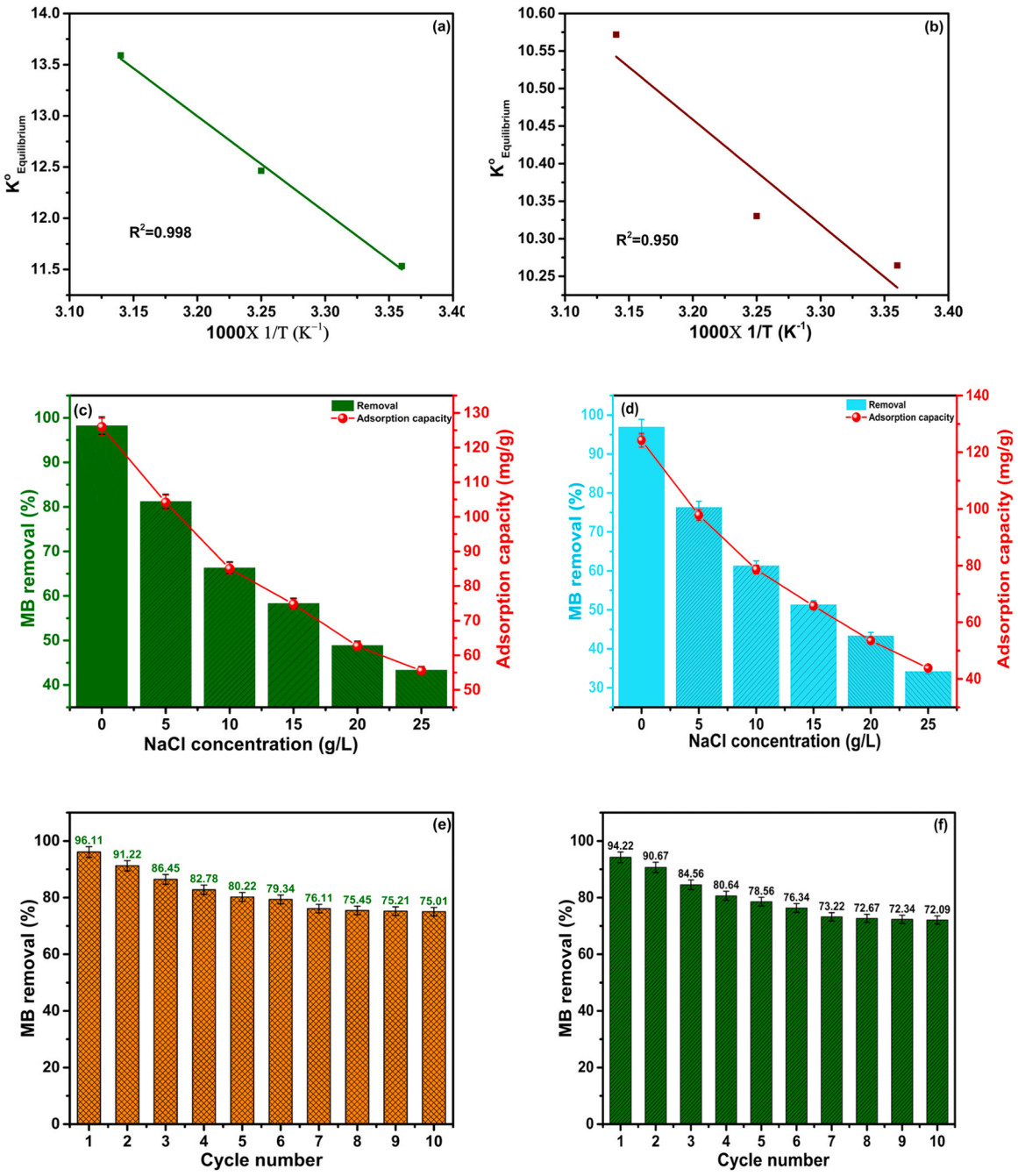

Fig. 8. Plots of (a-b) thermodynamics, (c-d) ionic strength, and (e-f) reusability studies of MB removal by CaO-ES@GO and CaO-FB@GO.

Table 3
Adsorption thermodynamic parameters for MB adsorption on CaO-ES@GO and CaO-FB@GO.

Adsorbent	T (K)	$\ln K^o_{Eq}$	ΔG^o (kJ mol^{-1})	ΔH^o (kJ mol^{-1})	ΔS^o (J mol^{-1} K^{-1})
	298	10.765	-26.343		
CaO-ES@GO	308	10.972	-28.962	21.680	261.825
	318	12.133	-31.580		
	298	11.533	-28.592		
CaO-FB@GO	308	12.464	-32.161	27.761	356.889
	318	13.591	-39.302		

CaO-FB@GO were 27.761 and 21.68, suggesting a physical adsorption, which was supported by the D-R model. Finally, the randomness increases in the MB concentration at the adsorbate-adsorbent interface was supported by the positive ΔS^o values (Ibrahim et al., 2023b).

3.6. *Effect of ionic strength*

The impact of ionic strength on the adsorption capacity and percentage removal of CaO-ES@GO and CaO-FB@GO on methylene blue

were tested using different concentrations of NaCl salt at optimum conditions of adsorbent dosage (0.4 g/L), initial MB concentration (50 mg/L), pH (8), contact time (60 min), and temperature (318 K). The results depicted in Fig. 8(c–d) for the adsorptive performance of CaO-ES@GO and CaO-FB@GO towards MB revealed a significant reduction in the sorption capacity and removal efficiency with increasing NaCl concentration. The finding suggests that dissolving NaCl in water resulted in the formation of Na^+, and as the NaCl concentration increased, more Na^+ was formed. As a result, the competition between the interfering Na^+ ions and cationic MB molecules on the surfaces of negatively charged CaO-ES@GO and CaO-FB@GO became greater, resulting in a significant decrease in MB removal efficiency and adsorption capacity (Yu et al., 2023). The existence of NaCl salts in MB solution during the adsorption process interfered with the establishment of electrostatic interaction between CaO-ES@GO and CaO-FB@GO surfaces and MB molecules (Alotaibi et al., 2023).

3.7. Stability study

The reusability study of CaO-ES@GO and CaO-FB@GO towards MB was examined to properly utilize their industrial application and cost effectiveness after several adsorption-desorption cycles. The CaO-ES@GO and CaO-FB@GO nanocomposites were regenerated after adsorption studies by desorbing MB from CaO-ES@GO and CaO-FB@GO surface after adsorption using an ethanol solution mixed with 5% acetic acid to boost the solvent polarity so it could destroy the electrostatic force between the MB and the nanocomposites. The mixtures were ultrasonicated for 10 min, washed repeatedly five times with distilled water, centrifuged at 2800 rpm, and dried in an oven for 3 h at 105 °C before being used for the next adsorption-desorption cycle. The results of the adsorptive performance of CaO-ES@GO and CaO-FB@GO towards MB during 10 successive cycles are shown in Fig. 8(e–f). As observed, the MB removal in the first cycle was 96.11% and 94.22% for CaO-ES@GO and CaO-FB@GO, respectively. However, between the second and tenth, a decrease in the MB removal from 91.22–75.01% for CaO-ES@GO and 90.67–72.09% for CaO-FB@GO (< 25%) was recorded. The outstanding reusability of the nanocomposites after 10 cycles can be attributed to the CaO containing GO, which were well preserved during the successive adsorption-desorption cycles. Furthermore, owing to their rapid adsorption kinetics, high stability, outstanding percentage removal, and suitability for MB adsorption, CaO-ES@GO and CaO-FB@GO may be a sustainable choice for the remediation of wastewater containing dye in water.

3.8. Practical application in real wastewater

In order to examine the practical application of CaO-ES@GO and CaO-FB@GO in real water samples, different water samples were collected from wastewater obtained from agricultural sources, sea water, distilled water, and tap water and spiked with MB solution (50 mg/L). The sorption process was carried out in a batch study at an adsorbent dosage of 0.4 g/L, pH = 8, MB initial concentration of 50 mg/L, contact time = 60 min, and volume of solution = 100 mL at 318 K (which are optimum conditions). The results demonstrated MB removal of 100%, 100% 98.88%, and 80.31% in tap water, distilled water, agricultural wastewater, and seawater for CaO-ES@GO, while 100%, 100%, 96.46%, and 76.34% were recorded for CaO-FB@GO, respectively. The lower MB percentage removal recorded for seawater could be attributed to the presence of soluble salts like calcium chloride and sodium chloride, which, when dissociated in aqueous solution, form positively charged cations (Mg^{2+} and Ca^{2+}). These positively charged cations compete for adsorption sites with the cationic MB on the surfaces of negatively charged CaO-ES@GO and CaO-FB@GO, leading to a decrease in MB removal.

3.9. Selective adsorption study

The needs to develop a highly selective adsorbent materials with high adsorptive performance for the simultaneous adsorption of cationic and anionic dyes from complex wastewater arises from the advantages of the materials. The adsorptive performance of CaO-ES@GO and CaO-FB@GO towards MB, RhB, and MO in a single component batch adsorption study is depicted in Fig. 9. In comparison of the dye color solutions after and before adsorption as presented in Fig. 9(a), it was observed that after adsorption, the color of MB was almost colorless, while a little change in color was observed for RhB and MO, demonstrating that the nanocomposites have strong affinity towards MB (Qiu et al., 2023). As depicted in Fig. 9(b), the CaO-ES@GO and CaO-FB@GO nanocomposites show good performance towards MB with uptake rates of 98.9% and 96.6%, respectively. In disparity, the adsorptive performance toward RhB and MO exhibits a noteworthy decrease under the same optimal conditions. This finding could be a result of electrostatic repulsion within the negatively charged dye structure and the negative adsorbent surface. Furthermore, during the sorption process, electrostatic attraction was promoted between the positively charged dyes and the negatively charged adsorbent surface (Yu et al., 2024). The significant decrease in the percentage removal of RhB could be attributed to their amphoteric nature, possessing both negative and positive charges (Meng et al., 2022). Moreover, under acidic conditions, the $–COO^-$ present in RhB is protonated (–COOH) and the cationic form ($N^+(C_2H_5)_2$) is left in the solution, thereby promoting electrostatic attraction between the positive charges of RhB. However, as the pH is increased (pH 8), a decrease in the RhB removal efficiency is observed. This observation can be attributed to the improved ionization of RhB at higher pH, resulting in the formation of more negatively charged ions, thereby leading to electrostatic repulsion between RhB and negatively charged adsorbent surfaces (Kohzadi et al., 2023).

The results of the binary mixture conducted to test the adsorptive selectivity of CaO-ES@GO and CaO-FB@GO towards cationic MB (target molecule), and RhB and MO as the competing molecules are as depicted in Fig. 10. The pictorial views in Fig. 10 (a, b, e, and f) demonstrate the binary mixtures of MB/RhB and MB/MO before and after adsorption onto CaO-ES@GO and CaO-FB@GO. A careful observation revealed that after adsorption, the color of MB in the solution disappeared, leaving behind the color that are in line with those of pure MO and RhB in the solutions (Zhang et al., 2023). This suggests the complete capture of cationic MB by CaO-ES@GO and CaO-FB@GO in the binary system. The plot of absorbance against wavelength for the two mixtures after and before adsorption by CaO-ES@GO and CaO-FB@GO is reported in Fig. 10 (c, d, g, and h). The maximum adsorption peaks related to MB were found to alter significantly following adsorption, while a small change was observed for RhB and MO, suggesting that CaO-ES@GO and CaO-FB@GO could favorably adsorb cationic MB (Thakkar et al., 2023). Finally, the separation efficiency of MB in the mixture of MB/RhB and MB/MO were 99.10% and 77.34% for GO@CaONPs-. ES and 61.23% and 47.81% for GO@CaONPs-FB, respectively, demonstrating that the CaO-ES@GO and CaO-FB@GO composites exhibited a higher adsorption selectivity towards cationic MB.

3.10. Adsorption mechanism

The interaction mechanisms governing the adsorptive behavior of CaO-ES@GO and CaO-FB@GO towards methylene blue were investigated by comparing the BET, SEM, AFM, XRD, FTIR, and XPS analyses after and before the sorption process. The BET surface area measurement decreased for CaO-ES@GO and CaO-FB@GO after MB adsorption from 121.14 m2/g to 72.81 m2/g; and 108.23 m2/g to 41.11 m2/g and, respectively. This decrease may be a result of the blockage of the adsorption active sites by MB molecules, suggesting the involvement of pore-filling mechanisms. The SEM images depicted in Fig. 11(a-b) in comparison showed the morphological structure of CaO-ES@GO and

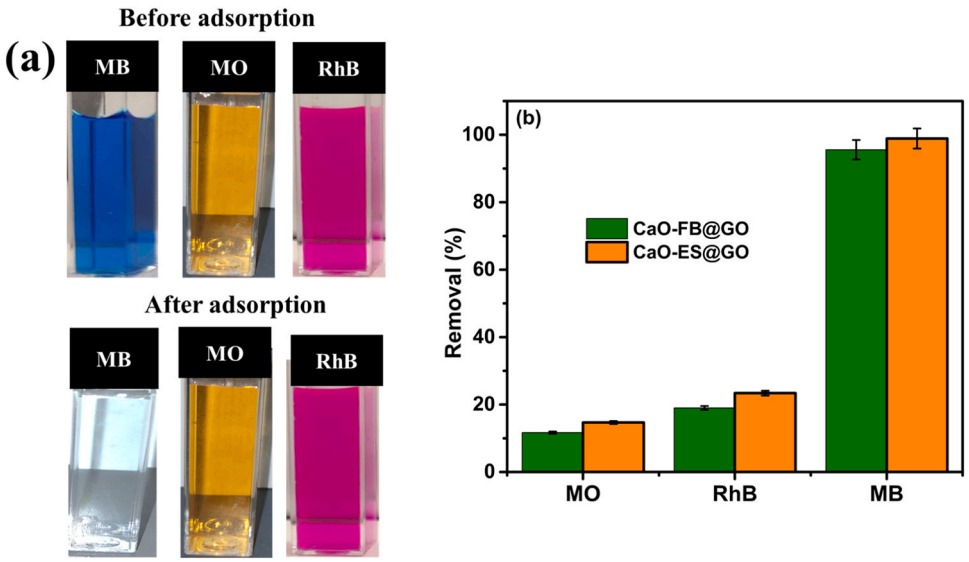

Fig. 9. (a) The pictorial view of MB, RhB, and MO before and after adsorption onto CaO-ES@GO and CaO-FB@GO in a single system and (b) MB, RhB, and MO removal on CaO-ES@GO and CaO-FB@GO nanocomposites.

CaO-FB@GO as not damaged after MB adsorption, indicating the occurrence of physical adsorption. The comparison of the AFM analysis before and after MB sorption for both composites as shown in Fig. 11(c-d), revealed that after MB sorption, the surface roughness of CaO-ES@GO and CaO-FB@GO had increased with increased average roughness from 110.7 nm to 210.2 nm, and 224.44 nm to 385.19 nm, respectively, suggesting the effective MB uptake of MB on the nanocomposite's surfaces.

The XRD pattern of CaO-FB@GO and CaO-ES@GO before and after uptake of methylene blue dye, as shown in Fig. 11(c), also revealed that there were no noticeable changes on the diffraction peaks. However, some sharp peaks were detected to have decreased in intensities after MB sorption, confirming that adsorption of MB on the surfaces of CaO-ES@GO and CaO-FB@GO is a surface phenomenon and, as supported by findings of SEM analysis and the D-R model, that the sorption process is directed and majorly dominated by physical adsorption (Yao et al., 2023). The FTIR spectra of CaO-ES@GO and CaO-FB@GO after and before adsorption with MB molecules, as presented in Fig. 11(d), demonstrated that there was no formation of new peaks and no peaks shifted. Moreover, the only change that was observed was that after MB adsorption onto CaO-ES@GO and CaO-FB@GO, the sharp and longer peak at 1149 cm^{-1}, which was attributed to C-O, was observed to be smaller. This observation could be due to the interaction between the carboxyl (C═O) and hydroxyl (O-H) with polar MB, resulting in the development of hydrogen bonding. The full XPS analysis spectrum of CaO-ES@GO and CaO-FB@GO after and before MB adsorption is depicted in Fig. 11(e). The results revealed the presence of carbon, oxygen, and calcium before adsorption, while sulphur and nitrogen were detected after adsorption, suggesting that MB molecules were adsorbed successfully onto the nanocomposite's surfaces (Ahmed et al., 2023a). The N 1 s high-resolution spectra of CaO-ES@GO and CaO-FB@GO after MB adsorption are presented in Fig. 11(f). The peak at 339.0 eV could be assigned to tertiary amine (-N =), while the visible peaks at 400.5 eV and 400.4 eV indicate the presence of quaternary ammonium (N +) (Liu et al., 2023b). Thus, the MB adsorption on CaO-ES@GO and CaO-FB@GO surfaces could be defined by an electron transfer process involving an N atom, governed by electrostatic attraction (Li et al., 2021). Furthermore, the S 2p high-resolution shown in Fig. 11(g) revealed peaks at 164.4 eV and 162.8 eV for CaO-ES@GO and also at 163.9 eV and 162.7 eV for CaO-FB@GO assigned to the spin-orbital of S 2p1/2 and S 2p3/2. The peaks formed between 164.4 eV and 163.7 eV could be as a result of hydrogen bond formation and C-S-S bond formation of MB molecules after the adsorption process (C-S-H), whereas the peaks located between 162.8 eV and 162.7 eV suggest the bond between the S-atom of MB molecules and the CaO-ES@GO and CaO-FB@GO oxygen atoms (Boughrara et al., 2022). The involvement of π -π interaction could result from the interaction between CaO-ES@GO and CaO-FB@GO surfaces and the aromatic rings of MB. In addition, the PZC of CaO-ES@GO and CaO-FB@GO by zeta potential were 5.10 and 5.6 before adsorption, while after MB adsorption, the PZC were observed to be 7.39 and 6.82 for CaO-ES@GO and CaO-FB@GO, respectively (Fig. 6(a-e)). The increased PZC after adsorption could be credited to the negatively charged adsorbent surfaces with increasing pH (pH>PZC), thereby promoting a strong electrostatic interaction between the positively charged cationic MB dye and negatively charged adsorbent surfaces (Ahmed et al., 2023b). These results revealed that the MB uptake towards CaO-ES@GO and CaO-FB@GO involve electrostatic interaction (Xie et al., 2023). Finally, interaction mechanism between MB molecules and CaO-ES@GO and CaO-FB@GO surfaces, as depicted in Fig. 12, is governed by the π -π interaction, electrostatic attraction, pore-filling, physical adsorption, and hydrogen bonding.

3.11. Comparative study

The adsorptive performance of CaO-ES@GO and CaO-FB@GO and their ability to remove MB were examined by comparing the absorption capacities with various reported adsorbents. The results (Table 4) revealed that the maximum sorption capacities of the developed nanocomposites towards MB were higher than those of some of the already reported adsorbents, suggesting their suitability and practical application in wastewater treatment in an aqueous environment.

3.12. Cost evaluation study

The various applications of sustainable nanocomposites for water remediation have prompted the necessity for cost evaluation to examine nanocomposites economic viability (GadelHak et al., 2023). As a result, the cost evaluation for the synthesis of CaO-ES@GO and CaO-FB@GO per gram for treatment of MB was calculated using several steps, such as the electricity cost consisting of the cost of heating, oven drying, ultrasonication, centrifugation, sample collection, etc. It was noticed from the results that CaO-ES@GO and CaO-FB@GO have a total production cost of approximately US$1.20/g and US$1.13/g, respectively (see Table S3). However, the material cost for treating 50 g/L MB in

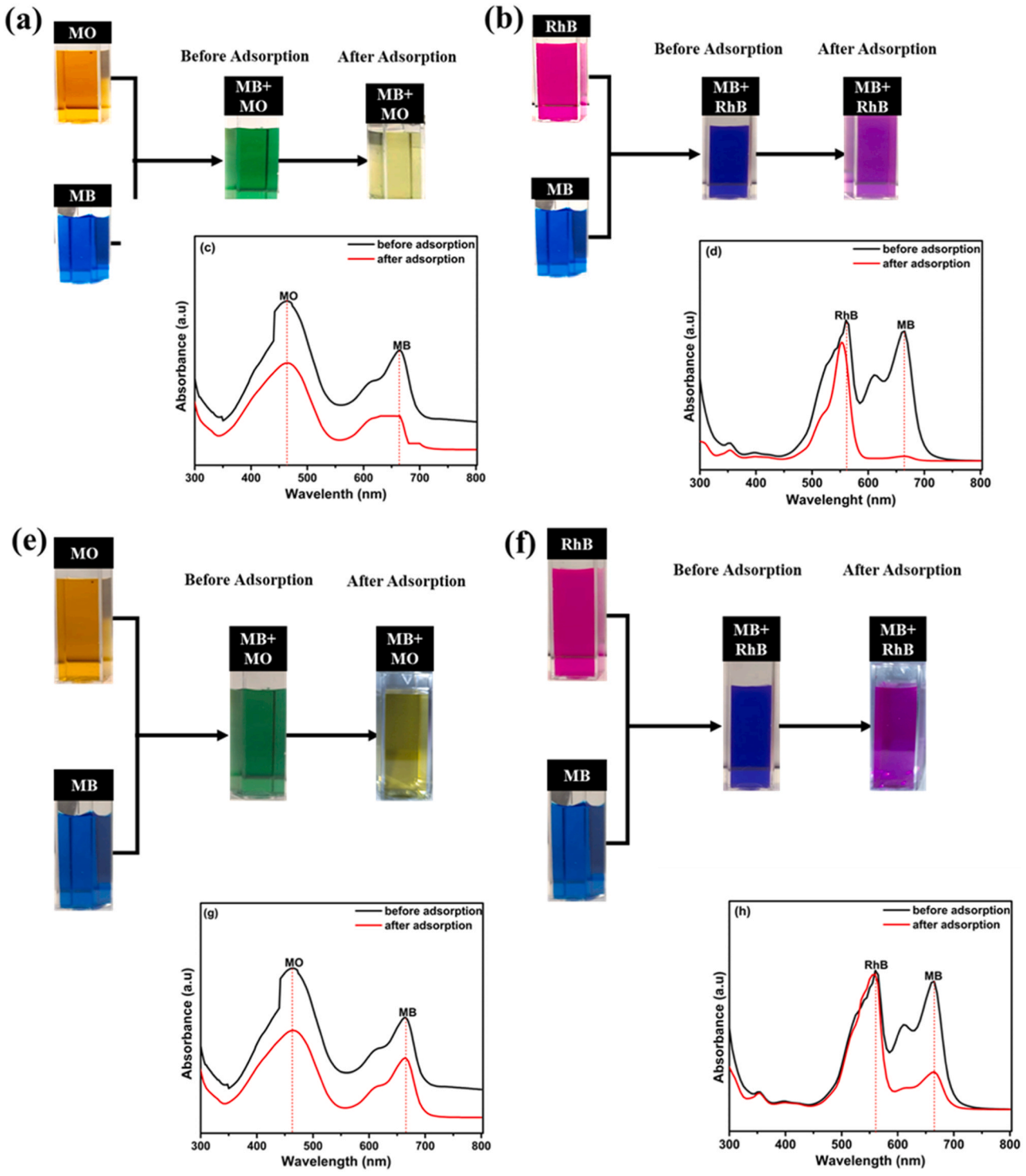

Fig. 10. The pictorial views and UV–vis adsorption spectra of MB/MO and MB/RhB binary mixtures before and after adsorption on CaO-ES@GO (a-d), and CaO-FB@GO(e-h).

100000 L of MB-containing wastewater was only US$48.00 and US $45.20, respectively. Nevertheless, with the utilization of CaO-ES@GO and CaO-FB@GO for 10 consecutive cycles with little usage and chemical costs for reuse, the cost will definitely drop to $4.80 and $4.52, respectively. This cost-benefit analysis demonstrates that the nanomaterials are sustainable, cost-effective, and have a high potential for use in real-life applications for the remediation of MB from an aqueous media. (Deb et al., 2022). The total production cost per gram in this study was relatively cheaper when compared with the work of Babakir et al. (2022), who reported the synthesis of P3ABA/GO/$CoFe^2O_4$ (US $2.96/g) for Congo red treatment.

3.13. Process optimization

3.13.1. Analysis of variance (ANOVA)

The experimental results depicted in Table S4 demonstrated that the lowest and highest percentages of MB removal were obtained in runs 3 and 10, which translated into 35.62% and 98.38% for CaO-ES@GO and

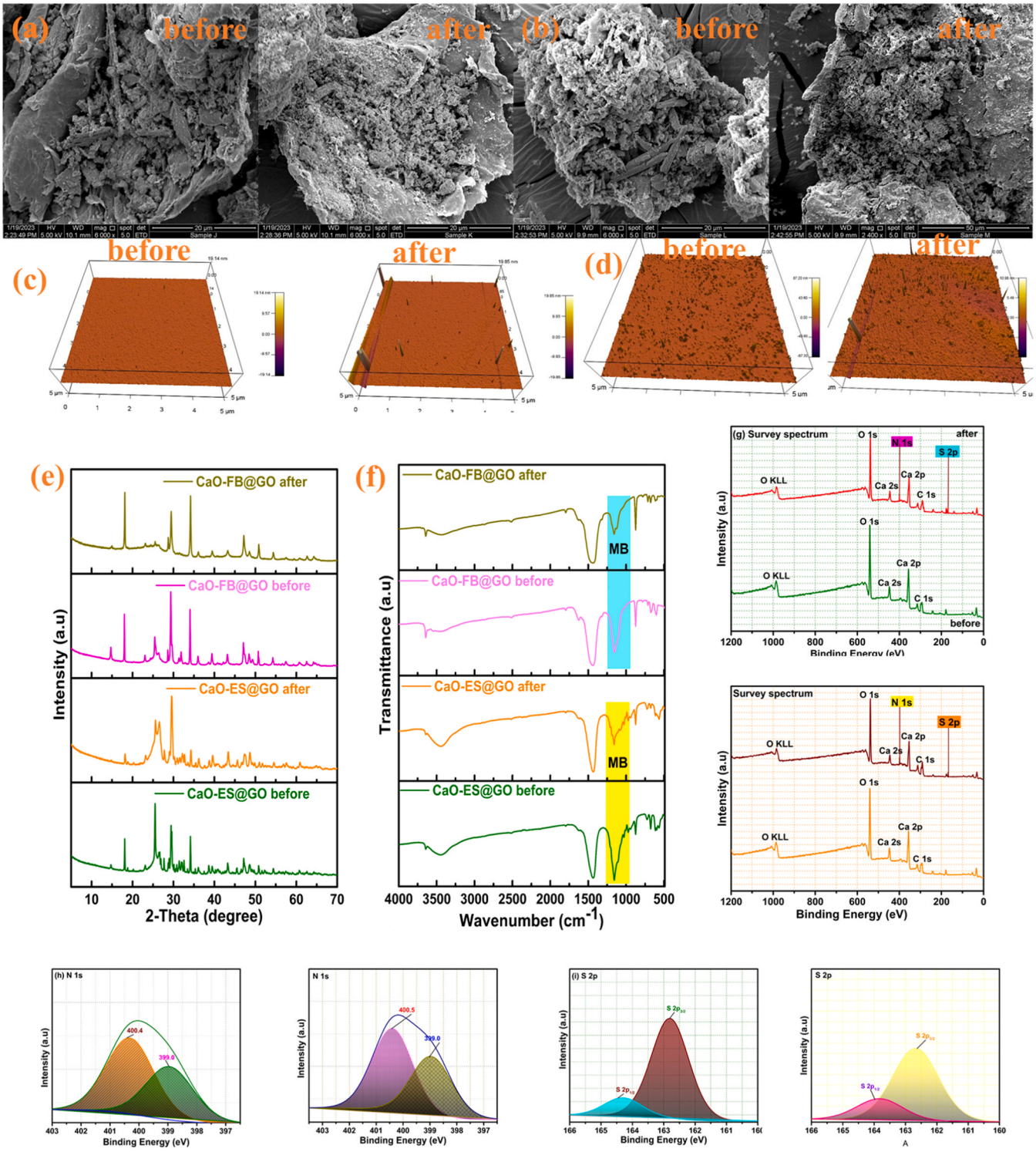

Fig. 11. SEM (a-b), AFM (c-d), XRD (e), FTIR (f), and XPS (g-i) analysis of CaO-ES@GO and CaO-FB@GO towards MB before and after adsorption.

32.94% and 96.80% for CaO-FB@GO, respectively. The ANOVA was engaged to evaluate the significance and consistency of the model. The ANOVA analysis for the adsorptive behavior of CaO-ES@GO and CaO-FB@GO towards MB is presented in Table S5. The quadratic model F-value and low P-value of 121.33 and < 0.0001 for CaO-ES@GO and 90.24 and $< 0.0001$for CaO-FB@GO suggest the significance of the model with P-values < 0.005. The lack of fit was observed to be insignificant, with P-values of 0.0510 and 0.1731 (> 0.05) for CaO-ES@GO and CaO-FB@GO, demonstrating the validity and suitability of the model. The model coefficient of variance (CV), adjusted R^2, regression coefficient (R^2), adequate precision, predicted R^2, standard deviation, and mean values for CaO-ES@GO and CaO-FB@GO are tabulated in Table S6. The R^2 of 0.991 and 0.983 suggest that the quadratic model selected can accurately predict approximately 99.1% and 98.3% of the experimental data, respectively. Further, the difference between the R^2-adjusted and R^2-predicted for CaO-ES@GO and CaO-ES@GO, which are < 0.15, suggests the applicability and reliability of the quadratic model (Kanani et al., 2022). The selected model was suggested to have high

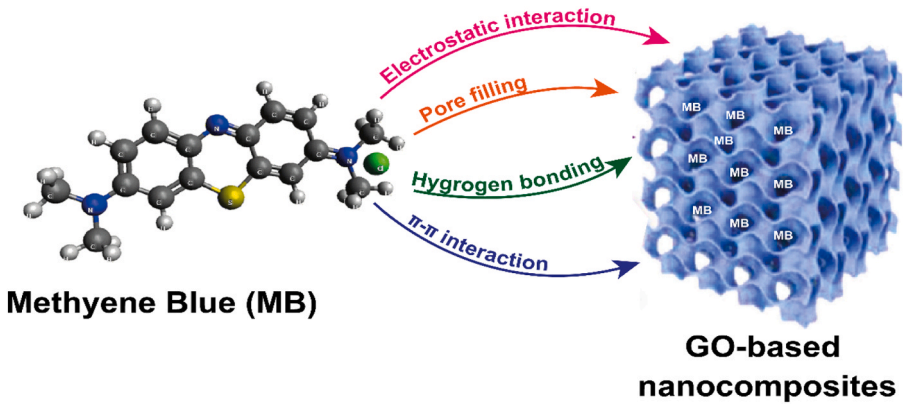

Fig. 12. Plausible adsorption mechanism of CaO-ES@GO and CaO-FB@GO towards MB adsorption.

Table 4
Maximum adsorption capacities of various adsorbents towards MB.

Adsorbent	Q_{max} (mg/g)	References
GO/CNF aerogel	111.2	Wang et al. (2021)
β-CD/GO	76.4	Yang et al. (2021)
Agar/GO/ZnO	33.3	Moradi et al. (2022b)
PGS–CS–GO	179.0	Rostamian et al. (2022)
KGM/GO/ZIF-67	219.8	Qiang et al. (2022)
MGO@Cellulose@Lipase	66.8	Mahmoud et al. (2022)
CaO-ES@GO	621.02	Present study
CaO-FB@GO	570.83	Present study
GOHNC	312.7	Sharma et al. (2022)
MSGO-4	260.9	Zhu et al. (2023)
GO-PLA	332.5	Nouri et al. (2023)
Fe3O4 @GO@AHSA	286.6	Alsohaimi et al. (2023)

precision and significant reproducibility judging from their CV values of 3.13% and 3.84% (10%) and adequate precision values of 36.62 and 33.5 (4.0) for CaO-ES@GO and CaO-FB@GO, respectively (Zalipour et al., 2022). In addition, the model suggests that among all the contributing variables under study for MB removal onto CaO-FB@GO and CaO-ES@GO, pH (69.90% and 71.04%) was observed to have the most significant effect, followed by temperature (27.55% and 26.62%) and adsorbent dosage (2.15%) and 2.34%). The quadratic regression model equations between the optimized variables and their corresponding responses is represented by Eqs. 10–11.

$$\mathrm{CaO-ES@GO} = +86.37 + 6.69A - 1.85B + 10.58C + 3.64AB + 1.78AC - 2.37BC + 3.73A^2 - 12.01B^2 - 20.86C^2 \quad (11)$$

$$\mathrm{CaO-FB@GO} = +80.23 + 6.74A - 2.00B + 11.02C + 4.00AB + 1.20AC - 2.03BC + 6.84A^2 - 11.55B^2 - 22.05C^2 \quad (12)$$

The model power transformation was investigated using the Box-Cox plots as depicted in Fig. S3(a–b). A model transformation is recommended if the current lambda (λ) values lie outside of the high- and low-confidence intervals (CI) (Miyah et al., 2021). The results obtained from the plots revealed that model transformation is not necessary since the current values of CaO-ES@GO (−0.15 and 1.67) and CaO-FB@GO (−0.38 and 1.33) lie between the confidence intervals. The plots of normal probability against internally and externally studentized residuals in Fig. S3(c-f) were observed to be distributed randomly, suggesting that the quadratic model for the adsorptive ability of CaO-FB@GO and CaO-ES@GO towards MB is very efficient in explaining and presenting real data.

3.13.2. *Three-dimensional plots: impact of contributing variables*

The 3-D plots presented in Fig. 10 demonstrate the combined contribution of pH, adsorbent dosage, and temperature to the uptake of MB by CaO-ES@GO and CaO-FB@GO. The synergistic effect of temperature and adsorbent dosage at constant pH on the removal of methylene blue by CaO-ES@GO and CaO-FB@GO is presented in Fig. 13 (a-b). The interaction temperature and adsorbent dosage on the sorption of MB on CaO-ES@GO and CaO-FB@GO offered the most significant contribution when compared to other interactions, as seen in the large F-values presented in Table S5. From the 3-D plots, maximum MB removal onto CaO-ES@GO and CaO-FB@GO was achieved with increasing temperature and adsorbent dosage. The rise in MB adsorption with a rise in temperature could be attributed to MB molecules diffusion and mobility increasing, which lowers the viscosity of the solution, suggesting an endothermic sorption process. The rise in the temperature of adsorption could also improve the porosity of CaO-ES@GO and CaO-FB@GO pores and enhance the accessibility of more active sites. However, further increases in adsorbent dosage beyond 0.4 g/L led to a decrease in MB sorption, and this could be elucidated by active site saturation at higher temperatures.

The interactive influence of temperature and pH at a fixed adsorbent dosage is presented in Fig. 13(c–d). As shown in the 3-D plots, the adsorptive behavior of CaO-ES@GO and CaO-FB@GO and MB removal increased with increased pH and temperature. As earlier reported, the PZC of CaO-ES@GO and CaO-FB@GO were 5.67 and 5.10, respectively. However, at PZC > pH, the surface of CaO-ES@GO and CaO-FB@GO becomes negatively charged, thereby enhancing an electrostatic attraction between the adsorbents and the positively charged MB at higher temperatures. The rise in temperature promoted the development of the adsorbent surface area and pores, which contributed to the sequestration of MB. The contribution of adsorbent dosage and pH at a constant temperature was demonstrated in Fig. 13(e–f). The results show that maximum uptake of MB on CaO-ES@GO and CaO-FB@GO was attained at an adsorbent dosage of 0.4 g/L and a pH of 8. This could be because the adsorbent surfaces are negatively charged with the presence of more active sites, which then attract the cationic MB molecules. However, increasing the pH and adsorbent dosage beyond this point resulted in a reduction in MB removal. This could be attributed to adsorbent particle aggregation and the competition of more H+ and cationic MB molecules in binding the COO- and OH- on the surfaces of CaO-FB@GO and CaO-ES@GO.

3.13.3. *Process optimization*

The desirability function is a powerful tool for process optimization studies because it allows multiple variables to be optimized simultaneously to achieve a specific response. This saves time, reduces costs, and avoids common challenges encountered when optimizing multiple variables independently. In this study, the desirability function was used

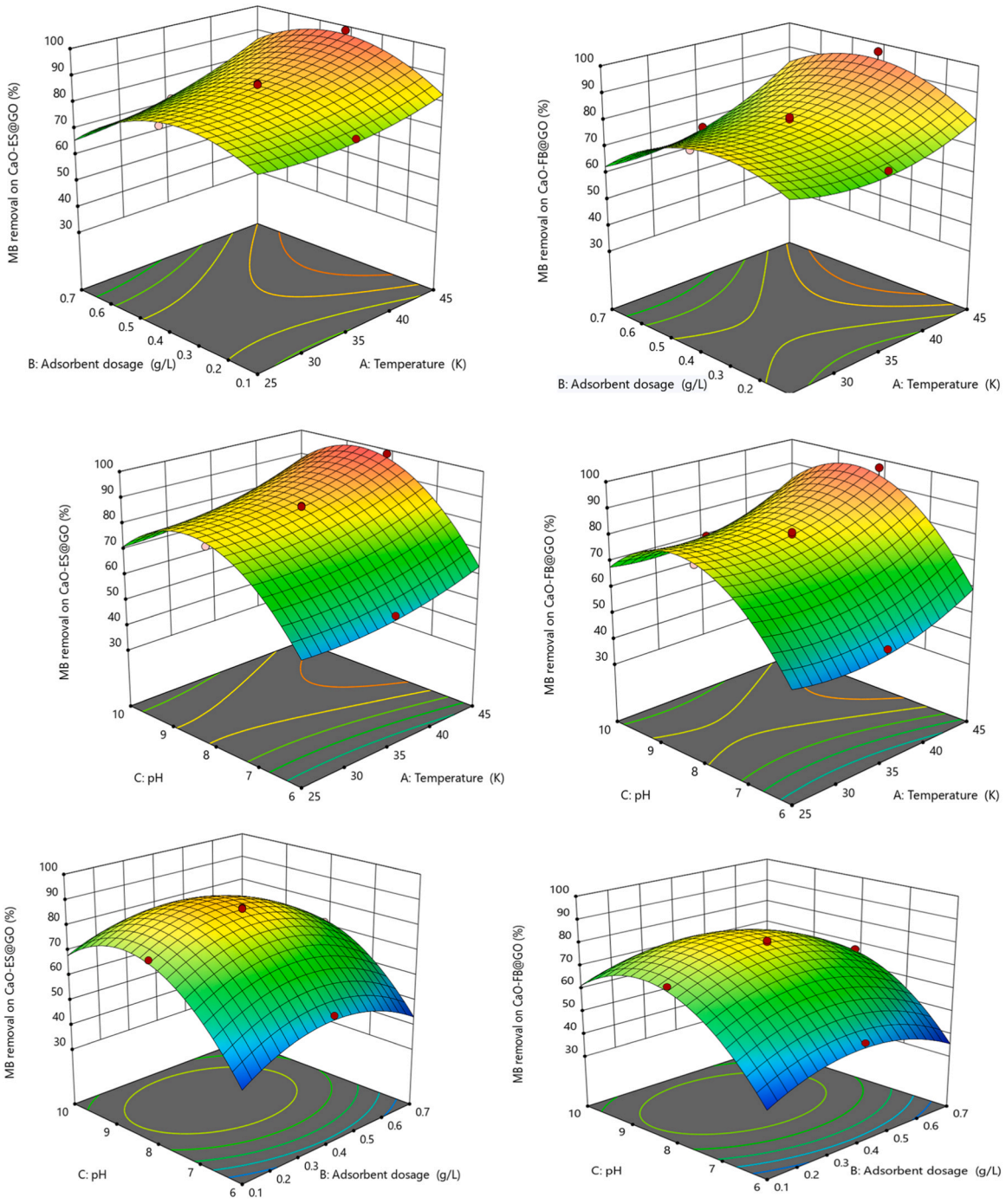

Fig. 13. Surface response plots for CaO-ES@GO and CaO-FB@GO towards MB removal: effect of (a-b) adsorbent dosage and temperature (c-d) pH and temperature (e-f) pH and adsorbent dosage.

to optimize the percentage removal of methylene blue dye on CaO-ES@GO and CaO-FB@GO. The design expert software was used to select the optimal conditions for the process, which were determined to be a pH of 8.55, an adsorbent dosage of 0.42, and a temperature of 318 K. The desirability of the process was set at 0.980. The MB removal onto CaO-ES@GO and CaO-FB@GO under these optimal conditions was found to be 96.79% and 93.82%, respectively. To confirm the applicability and suitability of the process, confirmatory experimentation was done in triplicate using the selected optimal variables. The values obtained for the percentage MB removal by CaO-ES@GO and CaO-FB@GO were 97.42% and 94.75%, respectively. The good synergy between the percentage MB removal values as predicted by the software and the experimental value under optimum conditions suggests the applicability of CCD for MB adsorption.

4. Conclusions

This study confirms the successful preparation of effective and sustainable eggshell and fishbone calcium oxide nanoparticles (CaONPs-ES and CaONPs-FB) loaded onto graphene oxide (CaONPs-ES@GO and CaONPs-FB@GO) via sol-gel and hydrothermal methods for the treatment of MB in aqueous environments. The successful loading of CaONPs on the GO surface was confirmed by SEM/EDX, XRD, FTIR, BET, and XPS techniques. SEM/EDX analysis revealed well-distributed CaO

nanoparticles on the GO surface. The mesoporous BET surface areas of synthesized CaONPs-ES@GO and CaONPs-FB@GO were 121 and 108 m^2/g, providing abundant adsorption sites for MB remediation. Various isotherm models were fitted to the equilibrium adsorption data of MB onto CaONPs-ES@GO and CaONPs-FB@GO, but the Redlich-Peterson model best represented the adsorption process, suggesting a combination of monolayer and multilayer adsorption predominantly dominated by multilayer adsorption on heterogeneous surfaces. The adsorption process behavior followed the pseudo-second order kinetic. Thermodynamics revealed that the adsorption process was primarily physical, spontaneous, and exothermic. Adsorption mechanism studies suggested that MB interaction with CaONPs-ES@GO and CaONPs-FB@GO was governed by π-π interaction, hydrogen bonding, pore-filling, and electrostatic interaction. Reusability tests revealed that nanocomposites demonstrated good performance (>70%) for MB treatment even after 10 successive cycles, making them suitable for practical applications. Cost analysis showed that CaONPs-ES@GO and CaONPs-FB@GO nanocomposites are economically viable for large-scale MB treatment applications. Optimum variables of temperature (318 K), adsorbent dosage (0.42 g/L), and pH (8.55) predicted by the model resulted in MB removal percentages of 97.42% and 94.75% for CaONPs-ES@GO and CaONPs-FB@GO, respectively. The agreement between predicted and experimental MB removal demonstrated the suitability of employing CCD, an aspect of RSM, for statistical analysis. In conclusion, synthesized CaONPs-ES@GO and CaONPs-FB@GO exhibited good thermal and structural stability, regenerability, reusability, and cost-effectiveness, making them promising and sustainable adsorbents recommended for industrial applications.

Declaration of Competing Interest

The authors declare that they have no known competing financial interests or personal relationships that could have appeared to influence the work reported in this paper.

Acknowledgements

The authors appreciate Curtin University Malaysia for providing research facility and financial support for the project. The authors also acknowledge Curtin Malaysia Postgraduate Research Scholarship (CMPRS) for the financial support. We also appreciate Global Centre for Environmental Remediation (GCER)'s laboratory and EMX unit, The University of Newcastle, Australia and the Surface Analysis Laboratory, MWAC, located at the University of New South Wales, Australia for instrumental support. The authors will also like to appreciate Institute of Sustainable Industries and Liveable Cities, Vic toria University, Australia. The immense contribution of Dr. Arghavan Mirahsani, Environmental Engineering Manager Grafoid Inc. Innovation Park, 945 Princess Street Kingston, Ontario, Canada is also appreciated.

Appendix A. Supporting information

Supplementary data associated with this article can be found in the online version at doi:10.1016/j.psep.2024.01.106.

References

Ahmadian, M., Jaymand, M., 2023. Interpenetrating polymer network hydrogels for removal of synthetic dyes: a comprehensive review. Coord. Chem. Rev. 486, 215152.
Ahmed, M.A., Mohamed, 2023b. Recent progress in semiconductor/graphene photocatalysts: synthesis, photocatalytic applications, and challenges. RSC Adv. 13, 421–439.
Ahmed, M.A., Mohamed, A.A., 2023a. A systematic review of layered double hydroxide-based materials for environmental remediation of heavy metals and dye pollutants. Inorg. Chem. Commun. 148, 110325.
Akdemir, M., Isik, B., Cakar, F., Cankurtaran, O., 2022. Comparison of the adsorption efficiency of cationic (Crystal Violet) and anionic (Congo Red) dyes on Valeriana officinalis roots: Isotherms, kinetics, thermodynamic studies, and error functions. Mater. Chem. Phys. 291, 126763.
Alizadeh, N., Salimi, A., 2023. Simultaneous adsorption and catalytic degradation of methylene blue dye over recyclable $Mn_4(P_2O_7)_3$ nanoflakes: Mechanism and efficiency, Environmental. Nanotechnol., Monit. Manag. 20, 100806.
Alotaibi, M.T., Mogharbel, R.T., Alorabi, A.Q., Alamrani, N.A., Shahat, A., El-Metwaly, N.M., 2023. Superior adsorption and removal of toxic industrial dyes using cubic Pm3n aluminosilica form an aqueous solution, isotherm, kinetic, thermodynamic and mechanism of interaction. J. Mol. Liq. 379, 121672.
Alsohaimi, I.H., Alhumaimess, M.S., Alqadami, A.A., Alshammari, G.T., Al-Olaimi, R.F., Abdeltawab, A.A., El-Sayed, M.Y., Hassan, M.H., 2023. Adsorptive performance of aminonaphthalenesulfonic acid modified magnetic-graphene oxide for methylene blue dye: Mechanism, isotherm and thermodynamic studies. Inorg. Chem. Commun. 147, 110261.
Anuma, S., Mishra, P., Bhat, B.R., 2021. Polypyrrole functionalized Cobalt oxide Graphene (COPYGO) nanocomposite for the efficient removal of dyes and heavy metal pollutants from aqueous effluents. J. Hazard. Mater. 416, 125929.
Asjadi, F., Yaghoobi, M., 2022. Characterization and dye removal capacity of green hydrothermal synthesized ZnO nanoparticles. Ceram. Int. 48 (18), 27027–27038.
Babakir, B.A.M., Ali, L.I.A., Ismail, H.K., 2022. Rapid removal of anionic organic dye from contaminated water using a poly(3-aminobenzoic acid/graphene oxide/cobalt ferrite) nanocomposite low-cost adsorbent via adsorption techniques. Arab. J. Chem. 15, 104318.
Bhagat, S.K., Pilario, K.E., Babalola, O.E., Tiyasha, T., Yaqub, M., Onu, C., E., Pyrgaki, K., Falah, M.W., Jawad, A.H., Yaseen, D.A., Barka, N., Yaseen, Z.N., 2023. Comprehensive review on machine learning methodologies for modeling dye removal processes in wastewater. J. Clean. Prod. 385, 135522.
Boughrara, L., Zaoui, F., Guezzoul, M., Sebba, F.Z., Bounaceur, B., Kada, S.O., 2022. New alginic acid derivatives ester for methylene blue dye adsorption: kinetic, isotherm, thermodynamic, and mechanism study. Int. J. Biol. Macromol. 205, 651–663.
Chandraraj, S.S., Xavier, J.R., 2023. Facile synthesis of graphene based mixed metal sulphide nanocomposite for energy storage applications. Surf. Interfaces 36, 102515.
Chen, D., Wang, Q., Li, Y., Li, Y., Zhou, H., Fan, Y., 2020. A general linear free energy relationship for predicting partition coefficients of neutral organic compounds. Chemosphere 247, 125869.
Dahlan, P., Keat, O.H., Aziz, H.A., Hung, Y.-T., 2023. Synthesis and characterization of MOF-5 incorporated waste-derived siliceous materials for the removal of malachite green dye from aqueous solution. Sustain. Chem. Pharm. 31, 100954.
Dan, S., Bagheri, H., Shahidizadeh, A., Hashemipour, H., 2023. Performance of graphene oxide/SiO_2 nanocomposite-based: antibacterial activity, dye and heavy metal removal. Arab. J. Chem. 16 (2), 104450.
Debnath, S., Das, R., 2023. Strong adsorption of CV dye by Ni ferrite nanoparticles for waste water purification: Fits well the pseudo second order kinetic and Freundlich isotherm model. Ceram. Int. 49 (10), 16199–16215.
Demirezen, D.A., Yılmaz, D.D., Yıldız, Y.S., 2023. Magnetic chitosan/calcium alginate double-network hydrogel beads: Preparation, adsorption of anionic and cationic surfactants, and reuse in the removal of methylene blue. Int. J. Biol. Macromol. 239, 124311.
Du, P., Zhang, J., Cai, Z., Ge, F., 2023. High adsorption of cationic dyes from aqueous solution using worm-like porous nanosilica: Isotherm, kinetics and thermodynamics, Materialstoday. Communications 35, 105697.
Garcia, J.L., Miyao, T., Inukai, J., Tongol, B, J.V., 2022. Graphitic carbon nitride on reduced graphene oxide prepared via semi-closed pyrolysis as electrocatalyst for oxygen reduction reaction. Mater. Chem. Phys. 288, 126415.
García-Soriano, D., Milán-Rois, P., Lafuente-Gómez, N., Navío, C., Gutiérrez, L., Cussó, L., Desco, M., Calle, D., Somoza, A., Salas, G., 2022. Iron oxide-manganese oxide nanoparticles with tunable morphology and switchable MRI contrast mode triggered by intracellular condition. J. Colloid Interface Sci. 613, 447–460.
Hammad, E.N., Salem, S.S., Mohamed, A.A., El-Dougdoug, W., 2022. Environmental impacts of ecofriendly iron oxide nanoparticles on dyes removal and antibacterial activity. Appl. Biochem. Biotechnol. 194 (12), 6053–6067.
Hu, J., Xu, Y., Zheng, X., Pan, Y., Wang, J., Shu, T., Wang, Y., Li, L., 2023a. Construction Iron-based metal organic frameworks based on ligand engineering for selective dyes removal from water solution. Inorg. Chem. Commun. 147, 110183.
Hu, N., Hang, F., Li, K., Liao, T., Rackemann, D., Zhang, Z., Shi, C., Xie, C., 2023b. Temperature-regulated formation of hierarchical pores and defective sites in MIL-121 for enhanced adsorption of cationic and anionic dyes. Sep. Purif. Technol. 314, 123650.
Hussain, A.A., Nazir, S., Khan, A.U., Tahir, K., Albalawi, K., Ibrahim, M.M., Almarhoon, Z.M., Al-Shehri, H.S., Mersal, G.A.M., Aldawsari, A.M., 2022. Preparation of zinc oxide graphted nickel incorporated mesoporous SBA-16 doped graphene oxide: an efficient catalyst for transesterification of waste edible oil to biodiesel and photocatalytic degradation of organic dyes. Inorg. Chem. Commun. 139, 109379.
Ibrahim, A.S., Gad, A.N., Dardeer, H.M., Gaber, A.-A., M., 2023a. Novel green biodegradable clarifying agents in sugar refining process using functionalized chitosan nanocomposites. Sustain. Mater. Technol. 35, e00525.
Ibrahim, S.M., Saeed, A.M., Elm 1 am, W.R.A., Mostafa, M.A., 2023b. Synthesis and characterization of new Schiff base bearing bis(pyrano[3,2-c]quinolinone): Efficient cationic dye adsorption from aqueous solution. J. Mol. Struct. 1284, 135364.
Januário, E.F.D., Fachina, Y.J., Wernke, G., Demiti, G.M.M., Beltran, L.B., Bergamasco, R., Vieira, A.M.S., 2022. Application of activated carbon functionalized with graphene oxide for efficient removal of COVID-19 treatment-related pharmaceuticals from water. Chemosphere 289, 133213.
Jawad, A.H., Saber, S.E.M., Abdulhameed, A.S., Farhan, A.M., ALOthman, Z.A., Wilson, L.D., 2023. Characterization and applicability of the natural Iraqi bentonite

clay for toxic cationic dye removal: adsorption kinetic and isotherm study. J. King Saud. Univ. - Sci. 35 (4), 102630.
Jia, Z., Wu, L., Han, C., Zhang, D., Li, M., Wei, R., 2023. Preparation of auto-suspending hollow silica microfiber derived from biotemplate and its highly selective adsorption for organic dyes, Materialstoday. Communications 34, 105437.
Kanani, M., Kanani, N., Batooie, N., Bozorgian, A., Barghi, A., Rezania, S., 2022. Removal of Rhodamine 6G dye using one-pot synthesis of magnetic manganese graphene oxide: Optimization by response surface methodology, Environmental. Nanotechnol., Monit. Manag. 18, 100709.
Kasirajan, R., Bekele, A., Girma, E., 2022. Adsorption of lead (Pb-II) using CaO-NPs synthesized by sol gel process from hen eggshell: Response surface methodology for modeling, optimization and kinetic studies. South Afr. J. Chem. Eng. 40, 209–229.
Khalili, R., Sabzehmeidani, M.M., Parvinnia, M., Ghaedi, M., 2022. Removal of hexavalent chromium ions and mixture dyes by electrospun PAN/graphene oxide nanofiber decorated with bimetallic nickel–iron LDH. Environ. Nanotechnol. Monit. Manag. 18, 100750.
Kim, S.-H., Kim, D.-S., Moradi, H., Chang, Y.-Y., Yang, Y.-K., 2023. Highly porous biobased graphene-like carbon adsorbent for dye removal: Preparation, adsorption mechanisms and optimization. J. Environ. Chem. Eng. 11 (2), 109278.
Kumar, J.A., Krithiga, T., Narendrakumar, G., Prakash, P., Balasankar, K., Sathish, S., Prabu, D., Pushkala, D.P., Marraiki, N., Ramu, A.G., Choi, D., 2022. Effect of Ca^{2+} ions on naphthalene adsorption/desorption onto calcium oxide nanoparticle: Adsorption isotherm, kinetics and regeneration studies. Environ. Res. 204, 112070.
Li, R., Tang, X., Wu, J., Zhang, K., Zhang, Q., Wang, J., Zheng, J., Zheng, S., Fan, J., Zhang, W., Li, X., Cai, S., 2023b. A sulfonate-functionalized covalent organic framework for record-high adsorption and effective separation of organic dyes. Chem. Eng. J. 464, 142706.
Li, W., Xie, Z., Xue, S., Ye, H., Liu, M., Shi, W., Liu, Y., 2021. Studies on the adsorption of dyes, methylene blue, safranin t, and malachite green onto polystyrene foam. Sep. Purif. Technol. 276, 119435.
Li, Z., Chen, Y., Wang, Z., Zhao, Y., Xia, Q., Qiu, J., Wang, H., Wang, J., 2023a. Ionic liquid hybrid metal–organic frameworks for efficient adsorption and selective separation of ammonia at high temperature. Chem. Eng. J. 464, 142728.
A. Liu S. He J. Zhang J. Liu W. Shao Preparation and char acterization of novel cellulose based adsorbent with ultra-high methylene blue adsorption performance Mater. Chem. Phys. 296 2023a 127261.
Liu et al., 2008Liu, W. , Huang, F. , Liao, Y. , Zhang, J. , Ren, G. , Zhuang, Z. , Zhen, J. , Lin, Z. , Wang, C. 2008. Treatment of CrVI-Containing Mg(OH)2 Nanowaste, Angewandte Chemie (International ed.), 47(30), 5619–5622.
Liu, Y., Yang, A.A., Zhang, X.-S., Sun, Z.-B., Li, W.-Z., Wang, Y., Luan, J., Liu, H.-C., 2022. Synthesis of metal–organic coordination polymers and their derived nanostructures for organic dye removal and analyte detection. J. Environ. Chem. Eng. 10 (4), 108215.
Liu, Z., Zhang, J., Zhang, L., Guan, Y., Ji, H., Zhang, Y., Gao, H., 2023b. Efficient removal of Congo red and methylene blue using biochar from Medulla Tetrapanacis modified by potassium carbonate. Bioresour. Technol. 376, 128912.
Lotfy, D., El-Sayyad, D.S., Shehata, N., 2023. Hexamethylenetetramine functionalized graphene oxide-alginate beads nanocomposite as efficient sorbent for dye from aqueous solution. Int. J. Biol. Macromol. 228, 754–772.
Lv, H.-W., Jiang, H.-L., He, F.-A., Hu, Q.-D., Zhong, R.-Z., Yang, Y.-Y., 2022. Adsorption of anionic and cationic dyes by a novel crosslinked cellulose-tetrafluoroterephthalonitrile-tannin polymer. Eur. Polym. J. 180, 111602.
Ma, J., Li, J., Weng, L., Ouyang, X., Chen, Y., Li, Y., 2023. Phosphorus-Enhanced and Calcium-Retarded Transport of Ferrihydrite Colloid: Mechanism of Electrostatic Potential Changes Regulated via Adsorption Speciation. Environ. Sci. Technol. 57 (10), 4219–4230.
Mahmoud, M.E., El-Sharkawy, R.M., Ibrahim, G.A.A., 2022. A novel bionanocomposite from doped lipase enzyme into magnetic graphene oxide-immobilized-cellulose for efficient removal of methylene blue and malachite green dyes. J. Mol. Liq. 368, 120676.
Maruthupandy, M., Muneeswaran, T., Anand, M., Quero, F., 2020. Highly efficient multifunctional graphene/chitosan/magnetite nanocomposites for photocatalytic degradation of important dye molecules. Int. J. Biol. Macromol. 153, 736–746.
Meng, S., Nan, Z., 2022. Rapid and selective adsorption of organic dyes with ultrahigh adsorption capacity using Na and Fe co-doped g-C_3N_4. Sep. Purif. Technol. 297, 121420.
Miyah, Y., Benjelloun, M., Lahrichi, A., Mejbar, F., Iaich, S., El Mouhri, G., Kachkoul, R., Zerrouq, F., 2021. Highly-efficient treated oil shale ash adsorbent for toxic dyes removal: Kinetics, isotherms, regeneration, cost analysis and optimization by experimental design. J. Environ. Chem. Eng. 9, 106694.
Moradi, O., Panahandeh, S., 2022a. Fabrication of different adsorbents based on zirconium oxide, graphene oxide, and dextrin for removal of green malachite dye from aqueous solutions. Environ. Res. 214, 114042.
Moradi, O., Pudineh, A., Sedaghat, S., 2022b. Synthesis and characterization Agar/GO/ZnO NPs nanocomposite for removal of methylene blue and methyl orange as azo dyes from food industrial effluents. Food Chem. Toxicol. 169, 113412.
Ndagijimana, P., Liu, X., Xu, Q., Li, Z., Pan, B., Wang, Y., 2022. Simultaneous removal of ibuprofen and bisphenol A from aqueous solution by an enhanced cross-linked activated carbon and reduced graphene oxide composite. Sep. Purif. Technol. 299, 121681.
A. Nouri W.L. Ang E. Mahmoudi S.F. Chua A.W. Mohammad A. Benamor M.M. Ba-Abbad C.P. Leo Decoration of polylactic acid on graphene oxide for efficient adsorption of methylene blue and tetracycline Chemosphere 322 2023 138219.
Obayomi, K.S., Lau, S.Y., Ibrahim, O., Zhang, J., Meunier, L., Aniobi, M.M., Atunwa, B.T., Pramanik, B.K., Rahman, M.M., 2023a. Removal of Congo red dye from aqueous environment by zinc terephthalate metal organic framework decorated on silver nanoparticles-loaded biochar: mechanistic insights of adsorption. Microporous Mesoporous Mater. 355, 112568.
Obayomi, K.S., Lau, S.Y., Mayowa, I.E., Danquah, M.K., Jianhua, Z., Chiong, T., Meunier, L., Rahman, M.M., 2023b. Recent advances in graphene-derived materials for biomedical waste treatment. J. Water Process Eng. 51, 103440.
Obayomi, K.S., Lau, S.Y., Danquah, M.K., Zhang, J., Chiong, T., Meunier, L., Gray, S.R., Rahman, M.M., 2023c. Green Synthesis of graphene-oxide based nanocomposites for efficient removal of methylene blue dye from wastewater. Desalination 564, 116749..
Obayomi, K.S., Lau, S.Y., Zahir, A., Meunier, L., Jianhua, Z., Dada, A.O., Rahman, M.M., 2023d. Removing methylene blue from water: a study of sorption effectiveness onto nanoparticles-doped activated carbon. Chemosphere 313, 137533.
Pai, S., Kini, M.S., Rangasamy, G., Selvaraj, R., 2023. Mesoporous calcium hydroxide nanoparticle synthesis from waste bivalve clamshells and evaluation of its adsorptive potential for the removal of Acid Blue 113 dye. Chemosphere 2023, 137476.
Pandey, D., Daverey, A., Dutta, K., Yata, V.K., Arunachalam, K., 2022. Valoriz. Waste pine Needle Biomass-.-. into biosorbents Remov. methylene blue Dye Water.: Kinet., Equilib. Thermodyn. Study, Environ. Technol. Innov. 25, 102200.
Princy, S.S.J., Hentry, C., Alodaini, H.A., Hatamleh, A.A., Arokiyaraj, S., Bindhu, M.R., 2023. Hibiscus cannabinus seeds assisted spherical silver nanoparticles and its antibacterial and photocatalytic applications. Chem. Phys. Impact 6, 100192.
Qasem, K.M.A., Khan, S., Chinnam, S., Saleh, H.A.M., Mantasha, I., Zeeshan, M., Manea, Y.K., Shahid, M., 2022. Sustainable fabrication of Co-MOF@CNT nano-composite for efficient adsorption and removal of organic dyes and selective sensing of Cr(VI) in aqueous phase. Mater. Chem. Phys. 291, 126748.
Qiang, T., Wang, S., Wang, Z., Ren, L., 2022. Recyclable 3D konjac glucomannan/graphene oxide aerogel loaded with ZIF-67 for comprehensive adsorption of methylene blue and methyl orange. J. Ind. Eng. Chem. 116, 371–384.
Qiu, C., Li, Y., Liu, H., Wang, X., Hu, S., Qi, H., 2023. A novel crosslinking strategy on functional cellulose-based aerogel for effective and selective removal of dye. Chem. Eng. J. 463, 142404.
Rasheed, S., Ali, G., Kousar, R., Raza, M.A., Kubra, K.T., Iftikhar, F.J., 2023. Synthesis and electrochemical performance evaluation of La doped TiO_2/reduced graphene oxide nanocomposites for supercapacitor application. J. Electroanal. Chem. 928, 117015.
Rheima, A.M., Khadom, A.A., Kadhim, M.M., 2022. Removal of cibacron blue P-6B dye from aqueous solution using synthesized anatase titanium dioxide nanoparticles: Thermodynamic, kinetic, and theoretical investigations. J. Mol. Liq. 357, 119102.
Rostamian, M., Hosseini, H., Fakhri, V., Talouki, P.Y., Farahani, M., Gharehtzpeh, A.J., Goodarzi, V., Su, C.-H., 2022. Introducing a bio sorbent for removal of methylene blue dye based on flexible poly(glycerol sebacate)/chitosan/graphene oxide ecofriendly nanocomposites. Chemosphere 289, 133219.
Sajjad, M., Ahmad, F., Shah, A.L., Khan, M., 2022. Designing graphene oxide/silver nanoparticles-based nanocomposites by energy efficient green chemistry approach and their physicochemical characterization. Mater. Sci. Eng. B 284, 115899.
Saleh, R., Taufik, A., 2019. Degradation of methylene blue and congo-red dyes using Fenton, photo-Fenton, sono-Fenton, and sonophoto-Fenton methods in the presence of iron(II,III) oxide/zinc oxide/graphene (Fe_3O_4/ZnO/graphene) composites. Sep. Purif. Technol. 210, 563–573.
Sangon, S., Hunt, A.J., Ngernyen, Y, Y., Youngme, S., Supanchaiyamat, N., 2021. Rice straw-derived highly mesoporous carbon-zinc oxide nanocomposites as high performance photocatalytic adsorbents for toxic dyes. J. Clean. Prod. 318, 128583.
Shaheen et al., 2023Shaheen, S. , Saeed, Z. , Ahmad, A. , Pervaiz, m ., Younas, M. , Khan, R.R.-M. , Luque, R. , Rajendran, S. ., 2023. Green synthesis of graphene-based metal nanocomposite for electro and photocatalytic activity; recent advancement and future prospective, Chemosphere, 311, 136982.
Shahraini, N., Entezari, M.H., 2022. Sonosynthesis of super-alkaline calcium-strontium oxide nanoparticles: size, morphology, and crystallinity affected the catalytic activity. Mater. Sci. Eng.: B 286, 116060.
Sharma, A.K., Dhiman, A., Nayak, A.K., Mishra, R., Agrawal, G., 2022. Environmentally benign approach for the efficient sequestration of methylene blue and coomassie brilliant blue using graphene oxide emended gelatin/κ-carrageenan hydrogels. Int. J. Biol. Macromol. 219, 353-36.
Singh, S., Naik, T.S.S.K., Anil, A.G., Khasnabis, S., Nath, B., Basavaraju, U., Kumar, V., Garg, V.K., Subramanian, S., Singh, J., Ramamurthy, P.C., 2022. A novel CaO nanocomposite cross linked graphene oxide for Cr(VI) removal and sensing from wastewater. Chemosphere 301, 134714.
Sree, G.V., Nagaraaj, P., Kalanidhi, K., Aswathy, C.A., Rajasekaran, P., 2020. Calcium oxide a sustainable photocatalyst derived from eggshell for efficient photo-degradation of organic pollutants. J. Clean. Prod. 270, 122294.
Thakkar, H., Bhatt, M., Thakore, S., 2023. Barbituric acid derived covalent organic framework and its CNT composite as high-performance adsorbents for organic dye removal. J. Environ. Chem. Eng. 11 (3), 109890.
Ullah, F., Ji, G., Irfan, M., Gao, Y., Shafiq, F., Sun, Y., Ain, Q.U., Li, A., 2022. Adsorption performance and mechanism of cationic and anionic dyes by KOH activated biochar derived from medical waste pyrolysis. Environ. Pollut. 314, 120271.
Vasiraja, N., Prabhahar, R.S.S., Joshua, A., 2023. Preparation and physio–chemical characterisation of activated carbon derived from Prosopis juliflora stem for the removal of methylene blue dye and heavy metal containing textile industry effluent. J. Clean. Prod. 397, 136579.
Vinayagam, R., Kandati, S., Murugesan, G., Goveas, L.C., Baliga, A., Pai, S., Varadavenkatesan, T., Kaviyarasu, K., Selvaraj, R., 2023. Bioinspiration synthesis of hydroxyapatite nanoparticles using eggshells as a calcium source: Evaluation of Congo red dye adsorption potential. J. Mater. Res. Technol. 22, 169–180.
Vo, T.S., Hossain, M.M., Lim, T.G., Suk, J.W., Choi, S., Kim, K., 2022. Modification of the interfacial glass fiber surface through graphene oxide-chitosan interactions for

excellent dye removal as an adsorptive membrane. J. Environ. Chem. Eng. 10 (6), 108965.
Wang, W., Song, L., Wang, Y., Zhang, X.F., Yao, J., 2021. Construction of a hybrid graphene oxide/nanofibrillated cellulose aerogel used for the efficient removal of methylene blue and tetracycline. J. Phys. Chem. Solids 150, 109839.
Wu, G., Zhou, G., Li, H., Xia, S., Zhu, Y., Han, J., Xing, W., 2023. Controlled fabrication of the biomass cellulose aerogel@ZIF-8 nanocomposite as efficient and recyclable adsorbents for methylene blue removal. Ind. Crops Prod. 193, 116169.
Xie, H., Yao, X., Yu, X., Mao, L., Zeng, Y., Wu, F., Guo, S., He, G., 2023. Flotation performance and adsorption mechanism of cerussite with phenylpropenyl hydroxamic acid collector. Minerals 13 (10), 1315.
Yadav, K., Latelwar, S.R., Datta, D., Jana, B., 2023. Efficient removal of MB dye using litchi leaves powder adsorbent: Isotherm and kinetic studies. J. Indian Chem. Soc. 100 (4), 100974.
Yadav, S., Asthana, A., Singh, A.K., Patel, J., Sreevidya, S., Carabineiro, S.A.C., 2022. Facile preparation of methionine-functionalized graphene oxide/chitosan polymer nanocomposite aerogel for the efficient removal of dyes and metal ions from aqueous solutions, Environmental. Nanotechnol., Monit. Manag. 18, 100743.
Yang, W., Cao, M., 2022. Study on the difference in adsorption performance of graphene oxide and carboxylated graphene oxide for Cu(II), Pb(II) respectively and mechanism analysis. Diam. Relat. Mater. 129, 109332.
Yang, Z., Liu, X., Liu, X., Wu, J., Zhu, X., Bai, Z., Yu, Z., 2021. Preparation of β-cyclodextrin/graphene oxide and its adsorption properties for methylene blue. Colloids Surf. B: Biointerfaces 200, 111605.
Yao, X., Yu, X., Wang, L., Zeng, Y., Mao, L., Liu, S., Xie, H., He, G., Huang, Z., Liu, Z., 2023. Preparation of cinnamic hydroxamic acid collector and study on flotation characteristics and mechanism of scheelite. Int. J. Min. Sci. Technol. 33 (6), 773–781.
Yu, H., Zhao, M., Xue, C., Huang, J., Zhao, N., Kong, L., 2024. All-solid-state Z-scheme nanojunction PW12/Ag/ZnO photocatalyst: Effective carriers transfer promotion and enhanced visible light driven. J. Mol. Struct. 1300, 137272.
Yu, X., Mao, L., Xie, H., Yao, X., He, G., Huang, Z., 2023. Flotation behavior and adsorption mechanism of phenylpropyl hydroxamic acid as collector agent in separation of fluorite from calcite. Langmuir 39 (16).
Zaki, A.H., Motagaly, A.T.A., Khaled, R., Lee, M.-J., Farghali, A.A., Shehata, N., 2022. Economic and facile approach for synthesis of graphene–titanate nanocomposite for water reclamation. J. Contam. Hydrol. 250, 104052.
Zalipour, Z., Lashanizadegan, A., Sadeghfar, F., Ghaedi, M., Asfaram, A., Sadegh, F., 2022. Electrochemical synthesis of CNTs–Zn: ZnO@SDS/PEG@Ni_2P nanocomposite and its application for ultrasound-assisted removal of methylene blue and investigation of its antibacterial property, Environmental. Nanotechnol., Monit. Manag. 18, 100721.
Zhang, X., Hou, L., Liu, H., Chang, L., Lv, S., Niu, B., Zheng, J., Liu, S., Fu, J., 2023. Hollow polyphosphazene microcapsule with rigid-flexible coupling cationic skeletons for highly efficient and selective adsorption of anionic dyes from water. Appl. Surf. Sci. 626, 157234.
Zhao, Y., Zhou, H., Song, M., Xu, Z., Sun, Z., Xu, Q., Chen, Y., Liao, X., 2023. Interface engineering of Ti-MOFs: adsorption of anionic, cationic and neutral dyes in wastewater. J. Mol. Struct. 1283, 135268.
Zhu, X., Zhou, G., He, G., Ma, L., Xu, B., Sun, F., 2023. Directly loading graphene oxide into melamine sponge for fast and high-efficiency adsorption of methylene blue. Surf. Interfaces 36, 102575.